

Density stratification controls the bedform phase diagram of saline-gravity currents versus open-channel flows

Authors: Koji Ohata^{1*}, Isabel de Cala², Robert M. Dorrell³, Hajime Naruse¹, Stuart J. McLelland³, Stephen M. Simmons³, William D. McCaffrey²

¹ Division of Earth and Planetary Sciences, Graduate School of Science, Kyoto University, Yoshidahonmachi, Sakyo Ward, Kyoto, 606-8501, Japan

² Institute of Applied Geosciences, School of Earth and Environment, University of Leeds, Woodhouse, Leeds, LS2 9JT, UK

³ Energy and Environment Institute, University of Hull, Cottingham Road, Hull, HU6 7RX, UK

* Corresponding author: Koji Ohata (ohata.koji.24z@gmail.com)

Associate Editor – Kyle Straub

Short Title – Bedform phase diagram for saline-gravity currents

Keywords: Bedforms, bedform phase diagram, density stratification, gravity currents, open-channel flows

This article has been accepted for publication and undergone full peer review but has not been through the copyediting, typesetting, pagination and proofreading process which may lead to differences between this version and the [Version of Record](#). Please cite this article as doi: [10.1111/sed.13075](https://doi.org/10.1111/sed.13075)

This article is protected by copyright. All rights reserved.

Accepted Article

ABSTRACT

Sedimentary bedforms such as ripples and dunes are generated both by river flows and sediment-laden gravity currents. Gravity current deposits are usually parameterized using existing bedform phase diagrams which are based on data from laboratory experiments and field observations of open-channel flows. Yet, it is not evident that open-channel flow bedform phase diagrams are applicable to gravity current deposits. Gravity current hydrodynamics are dependent on vertical density variation, i.e. density stratification, and therefore are fundamentally different from open-channel flows. New experiments to produce gravity current deposits are conducted and compared to existing open-channel flow data. It is shown that a parameter phase-space based on the lower layer of stratified gravity currents (i.e. that part below the velocity maximum) significantly improves the prediction of bedform type compared to bedform phase diagrams derived from layer-averaged parameters. These results confirm that bedforms produced by gravity currents can only be accurately predicted using the characteristics of the lower layer of stratified flow.

INTRODUCTION

Bedforms are topographic features produced by interactions between flow and sediment transport. They are observed in various natural settings such as rivers (e.g. Hendershot *et al.*, 2016), deserts (e.g. Lancaster, 1988), and snowpack (e.g. Filhol and Sturm, 2015). Further, extraterrestrial bedforms have been found on Mars, Venus, Titan, and Pluto (e.g. Telfer *et al.*, 2018). Relationships among the flows, sediment particles, and bedforms have been investigated for over a century (Owens, 1908). Empirical knowledge of bedforms is needed to predict risk in river engineering (e.g. Ashworth *et al.*, 2000). Because sedimentary structures, such as cross-lamination and parallel lamination, are recorded in deposits produced by the movement of bedforms (Harms, 1979), bedforms recorded in deposits also provide an archive of palaeoflow conditions. Based on laboratory and field observations, the relationships between hydraulic conditions and bedforms have been described via bedform phase diagrams for open-channel flows (e.g. van den Berg and van Gelder, 1993; Ohata *et al.*, 2017).

As well as rivers, dilute submarine gravity currents, such as turbidity currents or saline flows, develop bedforms (e.g. Flood *et al.*, 2009; Hughes Clarke, 2016; Hage *et al.*, 2018). Turbidity currents are particle-laden flows that are principal agents for transport of sediments from continental shelves to deep seas. These currents may erode and deposit significant amounts of sediments and thereby create deep-sea landscapes, for example, submarine canyons and submarine fans (e.g. Normark *et al.*, 2002; Dorrell *et al.*, 2015; Tubau *et al.*, 2015). Turbidity currents also transport organic carbon (Galy *et al.*, 2007; Liu *et al.*, 2012) and microplastics into deep seas (Kane and Clare, 2019). Deposits of turbidity currents (i.e. turbidites) are often observed in outcrops (e.g. Brooks *et al.*, 2018; Cornard and Pickering, 2019), and may exhibit cross-lamination and parallel

lamination (Bouma, 1962). In order to analyze turbidites, Baas *et al.* (2000) utilized a bedform phase diagram for open-channel flows.

Although submarine gravity currents are analogous to subaerial open-channel flows in terms of the ability to create bedforms and landscapes, the hydraulic properties of gravity currents differ from those of open-channel flows. For example, the density contrast of flows to ambient fluids is largely different between typical submarine gravity currents and open-channel flows. As a result, Kelvin-Helmholtz instability can occur at the upper boundary surfaces of gravity currents, while those of open-channel flows are stable due to a large density difference between air and water (Britter and Simpson, 1978). The interface instabilities lead the ambient water entrainment into the gravity currents.

As a result of ambient water entrainment, the vertical velocity structure of the flow is largely different between open-channel and turbidity currents. Velocity of open-channel flows monotonically increases with height (Fig. 1A), and the velocity profile in the near-bed region follows a logarithmic law (Nezu and Rodi, 1986). In contrast, the velocity of gravity currents reduces to zero at both the bed and the interface with ambient fluids (Fig. 1B).

The height of the velocity maximum, H_m , naturally separates gravity currents into lower and upper shear layers (Altinakar *et al.*, 1996; Xu, 2010; Dorrell *et al.*, 2019). In this paper, the regions below and above H_m are referred to as the 'lower layer' and 'upper layer', respectively (Fig. 1B). Previous experiments have shown that over short time and length scale flow velocity in the lower layer develops a logarithmic profile and that in the upper layer has a Gaussian-like profile (e.g. Kneller *et al.*, 1999; Hosseini *et al.*, 2006). Over long time and length scale, inherent to natural gravity currents, these

profiles do not necessarily hold (Dorrell *et al.*, 2019).

Despite its bipartite velocity structure, the mechanics of gravity currents have been often parameterized by the variables that are averaged from the bed to the ambient interface for simplicity (e.g. Ellison and Turner, 1959; Parker *et al.*, 1986). Hereafter, the layer represented using the layer-averaged parameters is referred to as the 'whole layer'. It should be noted, however, that gravity currents would be predicted to thicken inordinately downstream due to the entrainment of ambient water using existing layer-averaged models of gravity currents (Luchi *et al.*, 2018). This means that the vertical structure of the flow should be included in the analysis to capture the mechanics of gravity currents.

Considering the difference in hydraulic conditions and resultant behaviours of flows, it is not evident that conditions for formation of bedforms beneath unidirectional open-channel flows are applicable to gravity current deposits. Technological advances have enabled more direct observations of submarine gravity currents and bathymetric surveys of their deposits in recent years (Dorrell *et al.*, 2014, 2016; Hughes Clarke, 2016; Paull *et al.*, 2018; Gales *et al.*, 2019; Vendettuoli *et al.*, 2019), but there is still a paucity of data pertaining to bedforms produced by gravity currents (Dorrell *et al.*, 2019). Physical experiments have provided some detail on the process of submarine bedform formation (Sequeiros *et al.*, 2010a; Fedele *et al.*, 2016; Koller *et al.*, 2017, 2019). However, further experimental data are required to enable a comparison with bedform development in open-channel flows and develop a new phase diagram applicable to bedform development beneath gravity currents.

This study conducted laboratory experiments to fill gaps in the existing experimental data to develop new bedform phase diagrams for saline-gravity

currents with dimensionless parameters as axes to explore relationships among bedform phases, sediment particles, and flow conditions. The effect of the vertical flow structure in saline-gravity currents was investigated using parameters that represent the whole layer and the lower layer in different bedform phase diagrams. Finally, discriminant analysis was performed to evaluate the similarity between bedform phase regimes in saline-gravity currents compared with open-channel flows. The outcome was used to establish improved bedform phase diagrams for saline-gravity currents, that significantly enhance our ability to reconstruct palaeo-flow conditions from sedimentary structures of turbidites (Ohata *et al.*, 2017) as well as understanding dynamics of gravity currents.

METHODS

Experimental setup

Experiments were carried out at the Total Environmental Simulator of the University of Hull, United Kingdom. The Total Environmental Simulator is 10 m long, 6 m wide and 1.8 m deep tank. An experimental flume (10 m long, 0.1 m wide, and 0.6 m deep) was submerged in the tank with a constant bottom slope (Fig. 2). A 15 cm thick sediment bed was placed in the flume. Sediment particles used to build the bed were urea-based plastic media with a specific gravity of 1.5. Two grades of plastic sediment were used, with a narrow grain-size distribution (Dorrell *et al.*, 2018), thus characterized by their respective median diameters D_{50} of 253.6 and 428.3 μm (Fig. 3; Table 1). A hopper filled with the sediments was located at the upstream end to replenish the bed. Salt and water were mixed in four mixing tanks using sump pumps before each run. The capacity of each mixing tank was 1 m^3 , and one of the tanks was used to feed the water-

salt mixture into the flume at a constant rate using a metered flow pump. The inlet flow discharge was controlled, via an inverter, by an in-house MATLAB code with a computer connected to the pump. Other mixing tanks were used to keep a constant head in the main mixing tank. A flow diffuser consisting of coarse gravel in a wire mesh was located at the upstream end to ensure the water-salt mixture was injected uniformly.

Velocity profiles were obtained at 7.6 m and 8.2 m from the inlet using Nortek Vectrino Profiler Acoustic Doppler Velocimeters (ADV; Nortek Group, Rud, Norway). In several runs, the ADVs were moved manually in the vertical direction to adjust the measurement height relative to the bed. See more details about the velocity measurements in the Data Processing section. Density profiles were collected using a peristaltic pump and a siphon system at 6.3 m from the inlet. The siphon system had 24 tubes, and the intervals of tubes were 1 cm (from the lowest to 12th tubes), 1.5 cm (from the 12th to the 18th tubes), 2 cm (from the 18th to the 21st tubes), and 4 cm (from the 21st to the top tubes). The syphon system was introduced into the flume for 2 to 3 minutes at intervals of 5 minutes. For each run, three to six sets of flow samples were collected. The saline density of collected samples was measured using density meters (Anton Paar, Austria). Videos of experiments were taken from the side walls using four underwater GoPro Hero 4 (GoPro, Inc., San Mateo, CA, USA) cameras positioned at different points along the flume. Red dye was introduced to the inflow in order to visualize the current.

A total of six runs was conducted. The experimental conditions are summarized in Table 2. The parameters that were changed among the experimental runs were the inlet discharge Q_{in} (1.5, 2.0 or 3.0 L/s), the bottom slope S (0.012 or 0.052, corresponding to 0.7 or 3.0 degrees), the median diameter of plastic sediment D_{50} (253.6 or 428.3 μm). The

temperature of ambient water and water-saline mixture ranged from 15 to 17 degrees Celsius. The saline density of mixing tanks was from 1060 to 1070 kg/m³. The sediment bed was manually flattened before each run.

Data Processing

Newly obtained experimental data

Hydraulic parameters characterizing saline-gravity currents were calculated based on velocity and density profiles (Fig. 4). Seven parameters were used to calculate dimensionless parameters for phase diagrams: the layer-averaged flow velocity U , the maximum velocity U_m , the bed-related shear velocity u_* (hereafter bed-related is omitted for simplicity), the layer-averaged flow thickness H , the distance above the bed H_m showing the maximum velocity, the whole-layer-averaged density of saline-gravity currents ρ_g , and the lower-layer-averaged density of saline-gravity currents ρ_{gL} . Figures 1B and 1C illustrate the typical velocity and density profiles associated with these hydraulic parameters.

To obtain velocity and density profiles characterizing experimental runs, time-averaged values were extracted from time series of measured values. The velocity profiles were measured at the condition where the bedform was fully developed in the case of ripples and dunes, following the procedure used in previous studies (Sequeiros *et al.*, 2010a; Fedele *et al.*, 2016). The bed condition was assumed to be fully hydraulically rough. These were necessary to compare our results with existing datasets. The bed parallel component of measured velocities was extracted and averaged over a period of 200 s where the syphon array was not placed into the flume. However, in the case where the antidune developed through an experimental run, the velocities were averaged at

the time series before the bedforms appeared, and the initial distance from the bed to the ADV probes was used to set the local height of measured velocity. This was because the suspended load was too dense at the condition where antidunes were fully developed. The densities were averaged over all sets of flow samples except for the first set of samples. The height of the siphon rakes was measured visually using the video recordings.

The whole-layer-averaged velocity U , flow thickness H and density ρ_g were defined by integration of profiles of parameters as follows (Ellison and Turner, 1959):

$$UH = \int_0^{\infty} u \, dz \quad (1)$$

$$U^2H = \int_0^{\infty} u^2 \, dz \quad (2)$$

$$\rho_g H = \int_0^{\infty} \rho_{g,i} \, dz \quad (3)$$

where U denotes the local flow velocity, and $\rho_{g,i}$ denotes the local density of flows. In this study, the whole-layer-averaged velocity U and flow thickness H were estimated using the empirical relationships (e.g. Sequeiros *et al.*, 2010b) because the full profiles of velocity were not measured. The whole-layer averaged density was computed as follows:

$$\rho_g = \frac{\int_{z_{\min}}^H \rho_{g,i} \, dz}{H - z_{\min}} \quad (4)$$

where z_{\min} is the lowest height measured by the siphon system.

The layer-averaged flow thickness H was estimated from the height of interface H_a between gravity current and ambient water. Sequeiros *et al.* (2010b) implied that the interface height defined by both the density and the velocity profiles of flows is proportional to the layer-averaged flow thickness of turbidity currents. Based on the empirical relationships

proposed by Sequeiros *et al.* (2010b), this study estimated the layer-averaged flow thickness H by $H = H_a/1.4$ where the height H_a was obtained from the density profiles (Fig. 4B). The height of interface H_a was set to the location where the density excess was zero.

The shear velocity u_* was calculated using the logarithmic law (e.g. Keulegan, 1938) given by:

$$\frac{u}{u_*} = \frac{1}{\kappa} \ln \left(\frac{z}{z_0} \right) \quad (5)$$

where κ is the von Kármán constant ($=0.4$) and z_0 is the bed roughness height. Equation 5 is rewritten to the semi-logarithmic form:

$$u = \frac{u_*}{\kappa} \ln z - \frac{u_*}{\kappa} \ln z_0 \quad (6)$$

By fitting the local velocity and its height with the least square regression method, the shear velocity u_* and the bed roughness height z_0 can be computed (Fig. 5). Flow variation over the distance between the two spatially offset ADV (Figs 9–13) yields variation in measurements of flow velocity (Fig. 5). It should be noted that each ADV can measure the flow velocity only in a vertical range of 3 cm. Therefore, the ADV that covers the near-bed region was chosen, and the shear velocity was calculated from the velocity profile in the lowermost region of the experimental flow below the height of velocity maximum. From Equation 6, estimates for shear velocity were made in the near-bed region, $0.01 < z < 0.02$ m, to avoid the near-bed viscous sublayer and the horizon near the maximum velocity where the velocity profile deviates from the logarithmic form. In cases where both ADVs partially cover this analysis range, the ADV that has longer interval in the domain ranging $0.01 < z < 0.02$ m was employed to provide an estimate for flow shear velocity.

To estimate bulk flow parameters, data collected has to be extrapolated: the layer-averaged flow velocity U , the maximum velocity U_m , and the height of velocity

maximum H_m were estimated using the following equations proposed by previous studies (e.g. Sequeiros *et al.*, 2010b):

$$U_m = Cz_m u_* \quad (7)$$

$$Cz_m = \frac{1}{\kappa} \ln \left(\frac{30H_m}{k_s} \right) \quad (8)$$

$$H_m = H(0.8 - 0.27Fr_d) \quad (9)$$

with:

$$Fr_d = \frac{U}{\sqrt{\frac{\Delta\rho}{\rho_a} gH}} \quad (10)$$

$$U = \frac{U_m}{1.3} \quad (11)$$

with the density data from density profile and the estimated H , the simplex search method was used to solve these Eqs 7 to 11.

Here, Cz_m denotes a Chezy friction coefficient based on the maximum velocity U_m and k_s is the grain roughness height estimated as $k_s = 30z_0$. The parameter Fr_d is the densimetric Froude number where $\Delta\rho (= \rho_g - \rho_a)$ denotes the density difference between the current and the ambient water, ρ_a denotes the density of ambient water, and g is the gravitational acceleration. Equations 7 and 8 were proposed by Sequeiros *et al.* (2010b) and Equation 9 was derived by Abad *et al.* (2011), for saline driven gravity currents. Equation 11 is the empirical relationship by Altinakar *et al.* (1996).

The lower-layer-averaged density ρ_{gL} was calculated by integration of density profile as follows:

$$\rho_{gL} = \frac{\int_{z_{\min}}^{H_m} \rho_{gi} dz}{H_m - z_{\min}} \quad (12)$$

Existing data of gravity currents

In addition to the experimental data of this study, the hydraulic parameters were calculated using the data reported by Koller (2016) and Fedele *et al.* (2016). Koller (2016) and Fedele *et al.* (2016) reported the layer-averaged flow velocity U , the flow thickness H , and density ρ_g calculated using the moment equations of Ellison and Turner (1959). Koller (2016) also provided the maximum velocity U_m , the height H_m , the shear velocity u_* , and the vertical profiles of velocity and density. In contrast, these parameters representing hydraulic conditions of the lower layer were not addressed in the dataset of Fedele *et al.* (2016). Therefore, hydraulic parameters of the lower layer for Fedele's experimental runs were needed to be estimated using empirical relationships.

Koller (2016) The flow parameters provided by Koller (2016) are the layer-averaged flow velocity U , the flow thickness H , the maximum velocity U_m , the height H_m , and the shear velocity u_* .

The parameters U , H , and layer-averaged density ρ_g were computed using the moment equations of Ellison and Turner (1959) in Koller (2016). Although Koller (2016) reported the layer-averaged density $\rho_{g'}$, ρ_g and ρ_{gL} were calculated based on the density profiles of Koller's experiments and used to obtain the dimensionless numbers.

Abad *et al.* (2011) proposed the vertical profile of excess density as follows:

$$\zeta_c = \begin{cases} 1 & (\text{Fr}_d < 0.38) \\ 2.59 \exp(-2.5 \text{Fr}_d) & (\text{Fr}_d \geq 0.38) \end{cases} \quad (13)$$

$$f_{\delta c} = \frac{2}{1 + \zeta_c} \quad (14)$$

$$f_{\delta} = \begin{cases} f_{\delta c} \frac{1 - \zeta}{1 - \zeta_c} & (\zeta_c < \zeta < 1) \\ f_{\delta c} & (\zeta \leq \zeta_c) \end{cases} \quad (15)$$

where ζ is the elevation normalized by H and ζ_c is the elevation below which the density is approximated to constant. The parameter f_{δ} is the normalized vertical variation of excess density and $f_{\delta c}$ is the value of excess density approximated to constant near the bed. The normalized excess density $f_{\delta L}$ in the lower layer was obtained by integration of Eq. 15.

The present study has tested the relationships for H_m and ρ_{gL} using Koller's experimental data (Figs 6 and 7). The comparison between the observed H_m and Eq. 9 shows that the data of Koller (2016) scattered within the data of Abad *et al.* (2011) (Fig. 6). Figure 7 shows the comparison of the submerged specific density in the near bed region R_b based on the density calculated from the vertical profile and estimated density using Eqs 9 and 13 to 15. The submerged specific density in the near bed region R_b was computed as follows:

$$R_b = \frac{\rho_s - \rho_{gL}}{\rho_{gL}} \quad (16)$$

Although the equations by Abad *et al.* (2011) slightly underestimated R_b , the data of Koller (2016) plotted along the identity line (Fig. 7). Figures 6 and 7 show that the empirical relationships can be used to estimate the hydraulic parameters; therefore, the above equations were used to estimate the parameters for the data of Fedele *et al.* (2016).

Fedele *et al.* (2016) reported the layer-averaged flow velocity U , the flow thickness H , and density ρ_g calculated using the moment equations of Ellison and Turner (1959). Further, Fedele *et al.* (2016) provided a Shields diagram using some data where the reliable estimates of shear velocity were obtained.

The maximum velocity U_m , the height H_m , and the density of lower layer ρ_{gL} are not reported in the dataset of Fedele *et al.* (2016). Therefore, U_m , H_m and ρ_{gL} of their experimental runs were estimated using Equations 11, 9 and 13 to 15, respectively. Shields numbers τ_* were read from the Shields diagram proposed by Fedele *et al.* (2016).

Existing data of open-channel flows

Dimensional parameters for open-channel flows were compiled from the literature. In the calculation of the shear velocity v_* for laboratory data, the side-wall effect was removed using the method of Chiew and Parker (1994) [see Ohata *et al.* (2017) for details], and then the bed component of shear velocity was computed. For the field data, the shear velocity was computed by $v_* = \sqrt{ghS}$. Here, h denotes the flow depth of open-channel flows.

Governing Parameters

Bedform phases were expressed in the space of dimensionless parameters that reflect the properties of flows and sediment particles (van den Berg and van Gelder, 1993; Ohata *et al.*, 2017). First, the hydraulic conditions of saline-gravity currents were examined with the sediment diameter and the mobility of bed particles. The following dimensionless parameters were employed to represent hydraulic conditions and sediment properties: the particle Reynolds number Re_p , Shields number τ_* and Froude number Fr . These parameters correspond to Re_{pg} , τ_{*g} and Fr_d in the case of saline-gravity currents.

The stability conditions of the gravity current bedforms were also investigated using the dimensionless flow velocity V^0 and flow thickness h^0 proposed by Southard and

Boguchwal (1990). To examine the effect of the vertical structure of saline-gravity currents, the dimensionless flow velocity and thickness that represent the whole layer (U^0, H^0) and lower layer (U_m^0, H_m^0) were employed.

Open-channel flows

The particle Reynolds number Re_p (Vanoni, 1974) is defined as:

$$Re_p = \frac{\sqrt{RgD_{50}}D_{50}}{\nu} \quad (17)$$

Here, ν denotes the kinematic viscosity of the fluid and R is the submerged specific density of the sediment for open-channel flows given as:

$$R = \frac{\rho_s - \rho_f}{\rho_f} \quad (18)$$

where ρ_s and ρ_f denote the densities of the sediment and the water.

The kinematic viscosity ν was assumed to be a function of temperature according to the relationship for clear water (van den Berg and van Gelder, 1993):

$$\nu = [1.14 - 0.031(T - 15) + 0.00068(T - 15)^2]10^{-6} \quad (19)$$

where T represents the water temperature in degrees Celsius. A value of 20°C was assumed for data where T was not reported.

Shields number τ_* and Froude number are defined as, respectively:

$$\tau_* = \frac{v_*^2}{RgD_{50}} \quad (20)$$

$$\text{Fr} = \frac{V}{\sqrt{gh}} \quad (21)$$

where V is the mean flow velocity. Flows with a Froude number larger than unity are referred to as Fr-supercritical flows, while flows with a $\text{Fr} < 1$ are referred to as Fr-subcritical flows.

Dimensionless flow velocity V^0 and flow thickness h^0 for open-channel flows are obtained as (Southard and Boguchwal, 1990):

$$V^0 = V \left(\frac{1}{\nu Rg} \right)^{\frac{1}{3}} \quad (22)$$

$$h^0 = h \left(\frac{Rg}{\nu^2} \right)^{\frac{1}{3}} \quad (23)$$

Saline-gravity currents

The particle Reynolds number for saline-gravity currents Re_{pg} is defined as (Sequeiros *et al.*, 2010a):

$$Re_{pg} = \frac{\sqrt{R_b g D_{50} D_{50}}}{\nu} \quad (24)$$

Here, the submerged specific density in the near bed region R_b is given as:

$$R_b = \frac{\rho_s - \rho_b}{\rho_b} \quad (25)$$

where ρ_b denotes the near-bed density of saline-gravity currents (Sequeiros *et al.*, 2010a). In this study, ρ_{gL} was employed as the near-bed density of the fluid. Therefore, R_b was computed as follows:

$$R_b = \frac{\rho_s - \rho_{gL}}{\rho_{gL}} \quad (26)$$

The kinematic viscosity ν was calculated using Equation 19, and ν of this study was set to $1.08 \times 10^{-6} \text{ m}^2\text{s}^{-1}$ ($T = 17^\circ\text{C}$). A value of 20°C was assumed for published data where T was not reported.

Shields number τ_{*g} is defined as (Sequeiros *et al.*, 2010a):

$$\tau_{*g} = \frac{u_*^2}{R_b g D_{50}} \quad (27)$$

The densimetric Froude number Fr_d is defined by Equation 10. It is suggested that the critical value of Fr_d can be non-unity because of the nonuniform vertical velocity and density profiles (Waltham, 2004; Huang *et al.*, 2009; Dorrell *et al.*, 2016; Wu *et al.*, 2019).

Dimensionless flow velocity U^0 and flow thickness H^0 for saline-gravity currents were obtained as:

$$U^0 = U \left(\frac{1}{\nu R_b g} \right)^{\frac{1}{3}} \quad (28)$$

$$H^0 = H \left(\frac{R_b g}{\nu^2} \right)^{\frac{1}{3}} \quad (29)$$

where the submerged specific density for saline-gravity currents R_g was computed as $R_g = (\rho_s - \rho_g)/\rho_g$. Dimensionless maximum flow velocity U_m^0 and flow thickness of lower layer H_m^0 of saline-gravity currents were given as:

$$U_m^0 = U_m \left(\frac{1}{\nu R_b g} \right)^{\frac{1}{3}} \quad (30)$$

$$H_m^0 = H_m \left(\frac{R_b g}{\nu^2} \right)^{\frac{1}{3}} \quad (31)$$

Bedform classification

Compiled data of open-channel flow bedforms were classified into five types: ripples, ripples/dunes, dunes, upper-plane beds, antidunes. Antidunes were assigned to the same class as in the original references. Upper-plane beds were assigned for the data of plane beds where Shields number exceeds the threshold of suspension (Ohata *et al.*, 2022). Ripples, ripples/dunes, dunes were classified using the criteria proposed in Lapotre *et al.* (2017).

Lapotre *et al.* (2017) developed a new scaling relation for ripple wavelength that allows us to distinguish ripples and dunes as follows:

$$\lambda^* = 2504 \chi^{\frac{1}{3}} \quad (32)$$

where:

$$\lambda^* = \frac{\lambda v_*}{\nu} \quad (33)$$

$$\chi = \text{Re}_* \sqrt{\tau_*} \quad (34)$$

Here, χ is Yalin number and Re_* is the shear Reynolds number, defined as:

$$\text{Re}_* = \frac{v_* D_{50}}{\nu} = \frac{v_*}{\sqrt{RgD_{50}}} \text{Re}_p \quad (35)$$

Accepted Article

The shear Reynolds number Re_* express the relation of the acting forces to the bed particles (Shields, 1936).

Based on Eqs 20 and 35, Eq. 34 is rearranged as:

$$\chi = Re_* \sqrt{\tau_*} = Re_p \tau_* \quad (36)$$

Lapotre *et al.* (2017) proposed that the data follow Eq. 32 are interpreted as ripples. The data with $\chi < 4$ follow Eq. 32, whereas the data with $\chi < 9$ have much larger λ^* than that predicted by Eq. 32. Therefore, bedwaves with $\chi < 4$, $4 \leq \chi \leq 9$, and $9 < \chi$ can be interpreted as ripples, transitional bedforms and dunes, respectively (Lapotre *et al.*, 2017).

The bedforms observed in the experiments of this study were classified on the basis of the length, shape, and migration direction of the bed waves. The data for ripples and dunes under saline-gravity currents by Koller (2016) were reinterpreted using Eq. 32 (Fig. 8). Figure 8 shows that the Yalin number of 9 seems to correspond to the boundary between ripples and dunes under saline-gravity currents. However, all data plotted along Eq. 32, thus the ripple and dune data of Koller (2016) were classified as ripples. Fedele *et al.* (2016) do not report the wavelength of bedforms. Therefore, compiled data of gravity-current bedforms by Fedele *et al.* (2016) were assigned to the same class as in Fedele *et al.* (2016).

Discriminant Analysis

The discriminant analysis was applied to identify the stability conditions of open-channel flow bedforms in the V^0-h^0 space. The discriminant analysis is a classical statistical method that has been used for classification problems in various research areas (e.g. AbuZeina and Al-Anzi, 2018; Mahmoudi and Duman, 2015; Zou *et al.*, 2019).

Recently, Ohata *et al.* (2017) employed discriminant analysis to classify bedform phase regimes. The discriminant analysis determines a function to categorize a set of parameters on the basis of given categorized sets of variables (Fukunaga, 1990). Here, the classification method using the Mahalanobis distance (De Maesschalck *et al.*, 2000) was employed to obtain the boundaries of bedform phase regimes. The Mahalanobis distance measures the distance in parametric space between a data point and a categorized group of data points. The mathematical definition of the Mahalanobis distance is as follows:

$$d_M(\mathbf{x}) = \sqrt{(\mathbf{x} - \boldsymbol{\mu})^T \boldsymbol{\Sigma}^{-1} (\mathbf{x} - \boldsymbol{\mu})} \quad (37)$$

Here, d_M denotes the Mahalanobis distance, \mathbf{x} is an observation vector, $\boldsymbol{\mu}$ is the mean vector of a group, a superscript T denotes the transpose of a vector, and $\boldsymbol{\Sigma}$ denotes the covariance matrix. A data point can be assigned to a categorized group that shows the shortest Mahalanobis distance among all groups. Thus, if the Mahalanobis distance of a data point of a type of bedforms (for example, ripples) shows the shortest distance to a group of other types of bedforms (for example, dunes), the data point will be regarded as misclassified data. The transitional bedforms between ripples and dunes were considered to be accurately classified when the Mahalanobis distance was shortest to ripples or dunes.

The discriminant analysis allows us to evaluate the accordance of the observed data with the bedform phase regimes of open-channel flows obtained by the discriminant analysis. In the discriminant analysis, the inaccuracy of the classification model fitted to the original data points is expressed as an error rate r_e (Efron, 1986). This study utilized the apparent error rate, that is the observed inaccuracy of the model, for observational data of open-channel flows vs. saline-gravity currents.

RESULTS

Bedforms

Two kinds of bedforms were observed in the present experiments: ripples and antidunes. Each of the different bedforms observed in the experimental runs is described below. In runs 6, 7, 9 and 10, bedforms were interpreted as ripples (Figs 9 and 10). Equation 32 was used to interpret these bedforms (Fig. 11) in this study. Although the bedforms observed in this study can be interpreted as ripples (the data with $\chi < 4$) or dunes (the data with $\chi > 4$), the wavelength is relatively smaller than bedforms under open-channel flows and the data plotted along Eq. 32. Therefore, the bedforms observed in runs 6, 7, 9 and 10 were classified as ripples in this study.

The bed configurations in runs 3 and 5 were recognized as antidunes. Figure 12 shows the temporal development of bedforms in Run 3. The bedforms initiated as configurations with long-wavelength ($h = 60\text{--}110$ cm) and symmetrical profiles, then slowly propagated downstream or became stationary. At the latter stage of Run 3, short-length waves ($h = 20\text{--}30$ cm) reworked or superimposed on the large-scale waves. In Run 5, the bedforms observed at the upstream end of the flume had steep stoss and gentle lee slopes, and migrated in an upstream-direction slowly (Fig. 13). At the downstream end, the bedforms were symmetrical and remained stationary. The wavelength and wave height of bedforms in Run 5 were larger than that of Run 3 (Figs 12 and 13). From the profiles and wavelength, the bedforms in runs 3 and 5 were classified as antidunes.

Bedform Phase diagram

The experimental data reported in this study and previous studies (Fedele *et al.*, 2016;

Koller, 2016) were compared with the existing observational data of open-channel flows. The bedform phase regimes were described in the following two-dimensional spaces: (i) Shields diagram ($Re_p-\tau_*$ and $Re_{pg}-\tau_{*g}$; Fig. 14); (ii) Froude diagram (Re_p-Fr and $Re_{pg}-Fr_d$; Fig. 15); (iii) Velocity-Depth diagram (V^0-h^0 , U^0-H^0 , and $U_m^0-H_m^0$; Fig. 16).

Shields diagram

The flume data were plotted onto Shields diagram where Re_p (Re_{pg}) and τ_* (τ_{*g}) are shown on the vertical and the horizontal axis, respectively, to investigate relationships between particle diameter and shear stresses (Fig. 14). Figure 14 shows that stability fields of bedforms produced by saline-gravity currents do not deviate largely from those of open-channel flows in the Shields diagram. The dune data of Fedele *et al.* (2016) plot above the criteria of the dune stability field proposed by Lapotre *et al.* (2017), while the stability conditions of ripples reported by Koller (2016) were mostly plotted below the criteria. However, the stability fields of antidunes and plane beds cannot be clearly distinguished in Fig. 12 for both saline-gravity currents and open-channel flows because the stability fields of these two bedforms show an overlap, although antidunes have relatively higher Shields number than upper plane beds.

Froude diagram

Figure 15 shows a plot of Fr versus Re_p for the data of open-channel flows and Fr_d versus Re_{pg} for the data of saline-gravity currents. The open-channel flow data demonstrates that most of the bedforms in the lower flow regime (lower-plane bed, ripples, and dunes) plot in a region ranging $Fr < 0.8$, and some dune data points with $D_{50} > 0.8$ mm have larger Fr than unity. In contrast, the upper-flow-regime bedforms

(upper-plane bed and antidunes) tend to have high Fr ranging from 0.5 to 4.3, and most of the data plot in $0.5 < Fr < 2$. However, the data of saline-gravity currents shows much higher Fr_d than Fr of open-channel flows. The lower-flow-regime bedforms of saline-gravity currents plot in $0.5 < Fr_d < 2.8$, and the upper-flow-regime bedforms plot in $1.2 < Fr_d < 2.3$.

Velocity-Depth diagrams

The velocity-depth diagrams of bedforms were described in the space of: (i) V^0 versus h^0 for open-channel flows and U^0 versus H^0 for saline-gravity currents (the whole layer velocity-depth diagram; Figs 16A and 17A); and (ii) V^0 versus h^0 for open-channel flows and U_m^0 versus H_m^0 for saline-gravity currents (the lower layer velocity-depth diagram; Figs 16B and 17B). Since the particle diameter of gravity-current bedforms ranges $2 < Re_p < 45$, the data of open-channel flows with $2 < Re_p < 45$ were used for both the velocity-depth diagrams. In addition, velocity-depth diagrams of bedforms were described for finer sediment ($Re_p, Re_{pg} \leq 11.37$; Fig. 16) and coarser sediment $Re_p, Re_{pg} > 11.37$; Fig. 16). The particle Reynolds number $Re_p = 11.37$ corresponds to the sediment with $D_{50} = 0.2$ mm and $R = 1.65$.

Figures 16 and 17 shows that the sequence of open-channel flow bedforms from ripples to dunes, upper-plane bed, and antidune as V^0 increases. In addition, most dune data plotted on the diagram for coarse sediment (Fig. 17). The sequence of gravity-current bedforms from ripples to dunes and antidunes were also observed, although the data from Fedele *et al.* (2016) shows the overlapping of the data points. Also, the data from Fedele *et al.* (2016) fall in a region where the data of open-channel flows are sparse (Figs 16 and 17).

Discriminant analysis

Applying discriminant analysis, the stability conditions of bedforms were obtained as illustrated in Figs 18 and 19. The total apparent error rates for open-channel flows are 0.14% and 0.12% for fine and coarse sediment, respectively (Table 3). The apparent error rates r_e of each bedform are summarized in Table 3. Figures 18 and 19 show the velocity-depth diagrams with the bedform phase regimes of open channel flows obtained by discriminant analysis. The experimental data of saline-gravity currents were plotted using U^0 versus H^0 (Figs 18A and 19A) and U_m^0 versus H_m^0 (Figs 18B and 19B).

As a result of discriminant analysis of experimental data based on the whole-layer averaged values, almost all data of saline-gravity currents fall in the ripple and ripple/dune regimes of open-channel flow (Figs 18A and 19A). Thus, all ripple data are correctly classified as is obvious ($r_e = 0$) (Tables 4 and 5). Most data of dunes and antidunes as well as plane beds, however, are misclassified to the fields of different bedforms.

In contrast, Figs 18B and 19B and Tables 4 and 5 demonstrate that the gravity-current bedforms compare more favourably to open-channel flow by using the lower-layer values U_m^0 and H_m^0 . The error rates of dunes and upper-plane beds significantly decrease from 0.5–1.0 to 0–0.38, respectively (Tables 4 and 5). Even though the error rate of antidunes does not improve well compared to the whole layer velocity-depth diagram, the data of antidunes plot closer to the antidune regime of open-channel flows in the lower layer velocity-depth diagram. In the case of fine sediment, the total error rate of the lower-layer diagram ($r_e = 0.4$) is almost the same as that of the whole-layer diagram

($r_e = 0.41$). In addition, r_e of ripples increases from 0 to 0.16 in the diagram for fine sediment (Table 4). These are because almost all data plot in ripple regime and therefore the error rate of ripple formed by turbidity currents is 0 in the whole layer velocity-depth diagram. In contrast, in the case of coarse sediment, the total error rate of the lower-layer diagram improved from 0.76 to 0.24 compared to the whole-layer diagram.

DISCUSSION

Comparison of phase regimes with open-channel flows

This study suggests that the parameters characterizing the lower layer of saline-gravity currents can be used to better understand the relationships between hydraulic conditions and gravity current bedforms, as shown in the lower layer velocity-depth diagram (Figs 18B and 19B). The agreement of phase regimes was found by discriminant analysis using Mahalanobis distances (Tables 4 and 5). Although the whole-layer-averaged parameters have been used to represent the hydraulic conditions of saline-gravity currents (e.g. Parker *et al.*, 1986), the velocity-depth diagram using the whole layer averaged-parameters for saline-gravity currents do not coincide with that of open-channel flows (Figs 18A and 19A). The velocity-depth diagram using the whole layer-averaged parameters (Figs 18A and 19A) indicates that the bedform phase diagrams for open-channel flows cannot be applied to gravity current bedforms. The velocity-depth diagram for open-channel flows overestimates the layer-averaged velocity of saline-gravity currents and mispredicts that ripples generally appear in laboratory-scale saline-gravity currents (Figs 18A and 19A, Tables 4 and 5). Koller (2016) and Koller *et al.* (2017) also compared their experimental data with existing bedform phase diagrams by Simons and Richardson (1966) and Southard and Boguchwal (1990) that were described

in parameter spaces using layer-averaged parameters. As a result of the comparison, the data of Koller (2016) and Koller *et al.* (2017) showed disagreements with these phase diagrams. Koller *et al.* (2017) argued that the disagreement stemmed from the difference in the vertical flow structure and bed materials (plastic or siliciclastic particles), although they did not address the role of the lower layer of saline-gravity currents in producing bedforms.

Also, the difference regarding ambient fluids between open-channel flows and saline-gravity currents results in the deviation of the formation condition in the Froude diagram (Fig. 15). The densimetric Froude number of saline-gravity currents is higher than the Froude number of open-channel flows, whereas dunes, upper-plane beds, and antidunes appear in saline-gravity currents at smaller velocities than in open-channel flows, as shown in the whole layer velocity-depth diagram (Figs 18A and 19A). The discrepancy of phase regimes in the Froude diagram was caused by the reduced gravity effect (Fedele *et al.*, 2016). The reduced gravity $(\Delta\rho/\rho)g$ takes a much smaller value than the gravity acceleration g because the density of the ambient water is not negligible with respect to that of saline-gravity currents. Therefore, the densimetric Froude number of saline-gravity currents cannot be estimated using the Fr diagram for open-channel flows. However, the densimetric-Froude diagram of this study that is based only on the data pertaining to gravity current bedforms can be employed as the bedform predictor for saline-gravity currents, as shown previously by Fedele *et al.* (2016).

Relation between consistency in bedform phase diagrams and flow dynamics

Inconsistency of bedform phase diagrams between open-channel flows and saline-

gravity currents suggests that vertical flow structure of saline-gravity currents is the key factor in determining the flow dynamics for generating bedforms. The velocity-depth diagram for the lower layer (Figs 18B and 19B) indicates that the characteristic length of saline-gravity currents with respect to bedform development is represented by the height showing the maximum velocity, whereas that of open-channel flows is the flow depth defined as the distance from the bed to the free surface. From the accordance of the bedform phase regimes in Figs 18B and 19B, it is inferred that the layer interface where the maximum velocity of saline-gravity currents is attained plays a role like the free surface of open-channel flows.

This might be because the lower layer of a gravity flow exhibits a boundary layer-like flow structure that is similar to open-channel flows. Thus, similar evolutionary and hydrodynamic processes occur during the development of bedforms by gravity currents. Morphodynamic feedbacks between gravity currents and bed evolution processes are caused in the conditions of bed shear stress and sediment transport rate analogous to open channel flows. As a result, the maximum velocity might be a better predictor of the bottom-related shear stress of the gravity currents than the layer-averaged velocity that is the result of both bottom and interface friction.

The analogous behaviour of the layer interface with the free surface was observed in the flume experiments (Fedele *et al.*, 2016) and in the field (Dorrell *et al.*, 2019). In open-channel flows, the free-surface undulations show out-of-phase and in-phase relation with dunes and antidunes, respectively. The phase relations between bedforms and the layer interface were also observed in some experimental runs of Fedele *et al.* (2016) [see figs 4A and 8A of Fedele *et al.* (2016)].

Further, Dorrell *et al.* (2019) showed that, for the low- Fr_d saline-gravity currents in

the Black Sea, the layer interface dipped over the crest of the small-amplitude bedforms, i.e. an out-of-phase relation. It was postulated that this internal interface acts like the free surface due to a sharp gradient of potential vorticity. After Dorrell *et al.* (2019), rapid variation in potential vorticity, driven by breaking of gravity waves at critical-layers, inhibits eddy transportation across such a layer, i.e. gravity wave elasticity prevents the mixing of transported materials. This process can be seen to be analogous to Rossby wave forcing of atmospheric jets (Baldwin *et al.*, 2007; Dritschel and McIntyre, 2008; Dorrell *et al.*, 2019). Therefore, the thickness of the lower layer of saline-gravity currents is stabilized, and the layer interface behaves similarly to the free surface over the bedforms.

The phase diagram using the hydraulic parameters not related to the H_m , shown in Fig. 14, demonstrates that the bedform stability conditions in saline-gravity currents exhibit good agreement with those of open-channel flows in the Shields diagram. Fedele *et al.* (2016) also reported that their experimental data fall in the prediction regimes of ripples and dunes, when comparing Shields numbers. This agreement of phase regimes can be accounted for by the dynamical mechanisms that transport the bed materials in open-channel flows and saline-gravity currents. Shields numbers have been employed to formulate the bed-load transport rate in open-channel flows (e.g. Meyer-Peter and Müller, 1948; Wong and Parker, 2006). For gravity currents, Sequeiros *et al.* (2010b) measured the bed-load transport rate in experimental gravity currents and discovered that the transport rate follows the relationships for open-channel flows proposed by Ashida and Michiue (1972) and Wong and Parker (2006). The accordance of the bed-load transport relations in both flows suggests that open-channel flows and gravity currents interact with the sediment bed through similar dynamical mechanisms

(Sequeiros *et al.*, 2010b). Therefore, the bedform phase diagrams of saline-gravity currents and open-channel flows coincide well in the Shields space (Fig. 14).

Although the analogy between the lower layer of gravity currents and open-channel is also recognized in the velocity profiles (Sequeiros *et al.*, 2010b), the density structures of both currents are different. Air has a small density relative to the water in the case of open-channel flows, whereas the density of the upper layer is not negligible with respect to the lower layer of gravity currents. Also, the gravity currents are vertically stratified with the density, which may have an influence on the flow dynamics Dorrell *et al.* (2014). These hydrodynamic deviations of gravity currents from the open-channel flows are not incorporated in the parametric space of the lower layer velocity-depth diagram. Fedele *et al.* (2016) pointed out that the hydraulic conditions of the lower layer are also significant in considering behaviour of dunes formed by gravity currents. Further observation is required to understand the relationships between the density field of gravity currents and bedforms.

CONCLUSIONS

This paper reports new experiments of bedform formation by saline-gravity currents over an erodible sediment bed. Based on these results and a dataset compiled from the literature, the bedform phase diagrams for saline-gravity currents are examined in dimensionless parameter spaces. For the first time it is shown that bedform development by saline-gravity currents can only be assumed to be equivalent to open-channel flows if dimensionless saline-gravity-current parameters are based on the lower layer of the flow (i.e. that part below the velocity maximum). These results imply that the lower layer of the flow is the principal control on saline-gravity-current

morphodynamics and hydrodynamics.

The new understanding of morphodynamic and hydrodynamic processes of saline-gravity currents demonstrated in the analysis of bedform phase space has significant implications for engineering and field geology. The erosion and scour risk that gravity currents pose to offshore infrastructure engineering should be parameterized in terms of estimates of the lower layer of flows. Moreover, the interpretation of gravity-current deposits using the phase diagram for open-channel flow should only be used with the flow velocity and thickness of the lower layer of gravity currents, not the entire flow as has been previously applied. This latter point is critical for interpreting the sedimentary record and accurately reconstructing palaeoflow regimes to predict sediment transport conditions. Previous work (e.g. Lowe, 1988) interpreting the evolution of submarine fans, the largest sedimentary landforms on our planet, can be erroneous and should be reinterpreted for hydraulic conditions in the lower layer of the depositing gravity currents.

The precise estimation of flow conditions based on sedimentary structures is valuable to verify recently developed methodologies for deep-sea sedimentology. In recent years, direct observations by ADCPs in submarine canyons have provided information on the velocity and thickness of turbidity currents (Paull *et al.*, 2018; Hughes Clarke, 2016). However, turbidity currents that occur more than a few times a year in the modern age do not necessarily exhibit the same characteristics as those that produced ancient turbidites only once every several hundred years (Clare *et al.*, 2014). It is possible that turbidity currents forming actual submarine fans are much larger in scale and less frequent than those observed in the modern submarine canyons. On the other hand, numerical inverse analysis methods have been recently developed to

reconstruct the past hydraulic conditions from the characteristics of turbidites (Lesshafft *et al.*, 2011; Parkinson *et al.*, 2017; Naruse and Nakao, 2021; Cai and Naruse, 2021). Those methodologies potentially estimate the past flow conditions from geological records, but they depend on the accuracy of numerical forward models. For validating those methods at the scale of actual submarine fans, independent methods such as the discriminant analysis of sedimentary structures (Ohata *et al.*, 2017) will become even more significant in future studies.

ACKNOWLEDGEMENTS

This research was funded by Japan Society for the Promotion of Science (JSPS) Grant-in-Aid for JSPS Fellows, JSPS Overseas Challenge Program for young researchers, The Turbidites Research Group, School of Earth and Environment, University of Leeds, UK (Sponsors: AkerBP, BP, ConocoPhillips, Equinor, Eni, Hess, Murphy, OMV, Oxy and Shell), Sediment Dynamics Research Consortium (Sponsors: INPEX, JAPEX, JOGMEC, JX Nippon Oil and Gas Exploration), the Leeds Anniversary Research Scholarship, and the Energy and Environment Institute, University of Hull, UK. We gratefully acknowledge Brendan Murphy at the Total Environment Simulator laboratory, University of Hull, Lee Wilson and the research staff at the University of Hull for their help to set up the experiments. The data that supports the findings of this study are available in Table 2 of this article and were cited from Fedele *et al.* (2016) and Koller (2016). The data of open-channel flows used for the analysis are summarized in the supplementary tables of this article. Unpublished data used for the analysis were cited from the dataset of Brownlie (2018). The reference refers to the supplementary tables. The authors declare that they have no competing interests. We appreciate the Associate

Editor Kyle Straub and two anonymous reviewers for their in-depth comments which greatly improved the manuscript.

Accepted Article

REFERENCE

- Abad, J.D., Sequeiros, O.E., Spinewine, B., Pirmez, C., Garcia, M.H., Parker, G., 2011. Secondary current of saline underflow in a highly meandering channel: experiments and theory. *Journal of Sedimentary Research*, 81, 787–813.
- Abdel-Fattah, S., Amin, A., Van Rijn, L.C., 2004. Sand transport in Nile River, Egypt. *Journal of Hydraulic Engineering*, 130, 488–500.
- AbuZeina, D., Al-Anzi, F.S., 2018. Employing fisher discriminant analysis for Arabic text classification. *Computers & Electrical Engineering*, 66, 474–486.
- Alexander, J., Bridge, J.S., Cheel, R.J., Leclair, S.F., 2001. Bedforms and associated sedimentary structures formed under supercritical water flows over aggrading sand beds. *Sedimentology*, 48, 133–152.
- Altinakar, M.S., Graf, W.H., Hopfinger, E.J., 1996. Flow structure in turbidity currents. *Journal of Hydraulic Research*, 34, 713–718.
- Ashida, K., Michiue, M., 1972. Study on hydraulic resistance and bed-load transport rate in alluvial streams (in Japanese). *Proceedings of the Japan Society of Civil Engineers*, 1972, 59–69.
- Ashworth, P.J., Best, J.L., Roden, J.E., Bristow, C.S., Klaassen, G.J., 2000. Morphological evolution and dynamics of a large, sand braid-bar, Jamuna River, Bangladesh. *Sedimentology*, 47, 533–555.
- Baas, J.H., Van Dam, R.L., Storms, J.E., 2000. Duration of deposition from decelerating high-density turbidity currents. *Sedimentary Geology*, 136, 71–88.
- Baird, D.C., 2010. Field adjustments of bed form phase diagrams, in: *2nd Joint Federal Interagency Conference*, Las Vegas, NV, pp. 1137–1145.
- Baldwin, M.P., Rhines, P.B., Huang, H.P., McIntyre, M.E., 2007. The jet-stream

- conundrum. *Science*, 315, 467–468.
- Barton, J.R., Lin, P., 1955. *A study of the sediment transport in alluvial channels*. Technical Report CEF55JRB2, Colorado State University, Fort Collins, Colorado.
- Blom, A., Ribberink, J.S., de Vriend, H.J., 2003. Vertical sorting in bed forms: Flume experiments with a natural and a trimodal sediment mixture. *Water Resources Research*, 39.
- Bouma, A.H., 1962. *Sedimentology of some flysch deposits: A graphic approach to facies interpretation*. Elsevier Scientific Publishing Company, Amsterdam.
- Bridge, J.S., Best, J.L., 1988. Flow, sediment transport and bedform dynamics over the transition from dunes to upper-stage plane beds: implications for the formation of planar laminae. *Sedimentology*, 35, 753–763.
- Britter, R.E., Simpson, J.E., 1978. Experiments on the dynamics of a gravity current head. *Journal of Fluid Mechanics*, 88, 223–240.
- Brooks, H.L., Hodgson, D.M., Brunt, R.L., Peakall, J., Hofstra, M., Flint, S.S., 2018. Deep-water channel-lobe transition zone dynamics: Processes and depositional architecture, an example from the Karoo Basin, South Africa. *GSA Bulletin*, 130, 1723–1746.
- Brooks, N.H., 1955. Mechanics of streams with movable beds of fine sand, in: *Proceedings of the American Society of Civil Engineers*, pp. 1–28.
- Brownlie, W.R., 2018. Digitized dataset from "compilation of alluvial channel data: laboratory and field" (version 1.0).
- Cai, Z., Naruse, H., 2021. Inverse analysis of experimental scale turbidity currents using deep learning neural networks. *Journal of Geophysical Research: Earth Surface*, 126, e2021JF006276.
- Cao, H.H., 1985. *Résistance hydraulique d'un lit à gravier mobile à penteraide: étude expérimentale*. Ph.D. thesis, Ecole Polytechnique Fédérale de Lausanne, Switzerland.

- Chiew, Y.M., Parker, G., 1994. Incipient sediment motion on non-horizontal slopes. *Journal of Hydraulic Research*, 32, 649–660.
- Chyn, S.D., 1935. *An experimental study of the sand transporting capacity of the flowing water on sandy bed and the effect of the composition of the sand*. Ph.D. thesis, Massachusetts Institute of Technology, Cambridge, Massachusetts.
- Clare, M.A., Talling, P.J., Challenor, P., Malgesini, G., Hunt, J., 2014. Distal turbidites reveal a common distribution for large (> 0.1 km³) submarine landslide recurrence. *Geology*, 42, 263–266.
- Colby, B.R., Hembree, C.H., 1955. *Computations of total sediment discharge, Niobrara River near Cody, Nebraska*. United States Government Printing Office, Washington, DC.
- Cornard, P.H., Pickering, K.T., 2019. Supercritical-flow deposits and their distribution in a submarine channel system, middle Eocene, Ainsa Basin, Spanish Pyrenees. *Journal of Sedimentary Research*, 89, 576–597.
- Costello, W.R., 1974. *Development of bed configuration in coarse sands*. Ph.D. thesis, Massachusetts Institute of Technology, Cambridge, Massachusetts.
- Culbertson, J.K., Scott, C.H., Bennett, J.P., 1972. *Summary of alluvial-channel data from Rio Grande conveyance channel, New Mexico, 1965-69*. Technical Report 562-J, Professional Paper, Washington, DC.
- Davies, T.R., 1971. *Summary of experimental data for flume tests over fine sand*. Technical Report, Department of Civil Engineering, University of Southampton, Southampton, England.
- De Maesschalck, R., Jouan-Rimbaud, D., Massart, D., 2000. The mahalanobis distance. *Chemometrics and Intelligent Laboratory Systems*, 50, 1–18.
- Dorrell, R., Peakall, J., Sumner, E., Parsons, D., Darby, S., Wynn, R., Āzsoy, E., Tezcan, D.,

2016. Flow dynamics and mixing processes in hydraulic jump arrays: Implications for channel-lobe transition zones. *Marine Geology*, 381, 181–193.
- Dorrell, R.M., Amy, L.A., Peakall, J., McCaffrey, W.D., 2018. Particle size distribution controls the threshold between net sediment erosion and deposition in suspended load dominated flows. *Geophysical Research Letters*, 45, 1443–1452.
- Dorrell, R.M., Burns, A.D., McCaffrey, W.D., 2015. The inherent instability of leveed seafloor channels. *Geophysical Research Letters*, 42, 4023–4031.
- Dorrell, R.M., Darby, S.E., Peakall, J., Sumner, E.J., Parsons, D.R., Wynn, R.B., 2014. The critical role of stratification in submarine channels: Implications for channelization and long runout of flows. *Journal of Geophysical Research: Oceans*, 119, 2620–2641.
- Dorrell, R.M., Peakall, J., Darby, S.E., Parsons, D.R., Johnson, J., Sumner, E.J., Wynn, R.B., Özsoy, E., Tezcan, D., 2019. Self-sharpening induces jet-like structure in seafloor gravity currents. *Nature Communications*, 10, 1381.
- Dritschel, D.G., McIntyre, M.E., 2008. Multiple jets as PV staircases: The Phillips Effect and the resilience of eddy-transport barriers. *Journal of the Atmospheric Sciences*, 65, 855–874.
- East Pakistan Water and Power Development Authority, 1966,1968-1969. Flume studies of roughness and sediment transport of movable bed of sand, Annual Report of Hydraulic Research Laboratory, Dacca.
- Efron, B., 1986. How biased is the apparent error rate of a prediction rule? *Journal of the American Statistical Association*, 81, 461–470.
- Ellison, T.H., Turner, J.S., 1959. Turbulent entrainment in stratified flows. *Journal of Fluid Mechanics*, 6, 423–448.
- Fedele, J.J., Hoyal, D., Barnaal, Z., Tulenko, J., Awalt, S., 2016. Bedforms created by gravity flows, in: David A. Budd, Elizabeth A. Hajek, S.J.P. (Ed.), *Autogenic Dynamics and*

- Self-Organization in Sedimentary Systems*, pp. 95–121.
- Filhol, S., Sturm, M., 2015. Snow bedforms: A review, new data, and a formation model. *Journal of Geophysical Research: Earth Surface*, 120, 1645–1669.
- Flood, R.D., Hiscott, R.N., Aksu, A.E., 2009. Morphology and evolution of an anastomosed channel network where saline underflow enters the black sea. *Sedimentology*, 56, 807–839.
- Foley, M.G., 1975. *Scour and fill in ephemeral streams*. Technical Report KH-R:KH-R-33, W. M. Keck Laboratory of Hydraulics and Water Resources, California Institute of Technology, Pasadena, California.
- Franco, J.J., 1968. Effects of water temperature on bed-load movement. *Journal of the Waterways and Harbors Division*, 94, 343–352.
- Fukunaga, K., 1990. *Introduction to Statistical Pattern Recognition (2nd Ed.)*. Academic Press Professional, Inc., San Diego, CA.
- Fukuoka, S., Okutsu, K., Yamasaka, M., 1982. Dynamic and kinematic features of sand waves in upper regime [in Japanese], in: *Proceedings of the Japan Society of Civil Engineers*, Japan Society of Civil Engineers, pp. 77–89.
- Gabel, S.L., 1993. Geometry and kinematics of dunes during steady and unsteady flows in the Calamus River, Nebraska, USA. *Sedimentology*, 40, 237–269.
- Gales, J.A., Talling, P.J., Cartigny, M.J.B., Hughes Clarke, J., Lintern, G., Stacey, C., Clare, M.A., 2019. What controls submarine channel development and the morphology of deltas entering deep-water fjords? *Earth Surface Processes and Landforms*, 44, 535–551.
- Galy, V., France-Lanord, C., Beyssac, O., Faure, P., Kudrass, H., Palhol, F., 2007. Efficient organic carbon burial in the Bengal fan sustained by the Himalayan erosional system. *Nature*, 450, 407–410.

- Gee, D.M., 1975. Bed form response to nonsteady flows. *Journal of the Hydraulics Division*, 101, 437–449.
- Gibbs, C.H., Neill, C.R., 1972. *Interim report on laboratory study of basket-type bed-load samplers*. Technical Report REH/72/2, Research Council of Alberta, Edmonton, Alberta, Canada.
- Gilbert, G.K., 1914. *The transportation of debris by running water*. Technical Report 86, Professional Paper, Washington, DC.
- Guala, M., Singh, A., BadHeartBull, N., Foufoula-Georgiou, E., 2014. Spectral description of migrating bed forms and sediment transport. *Journal of Geophysical Research: Earth Surface*, 119, 123–137.
- Guy, H.P., Simons, D.B., Richardson, E.V., 1966. *Summary of alluvial channel data from flume experiments, 1956–61*. Technical Report 462-I, Professional Paper, Washington, DC.
- Hage, S., Cartigny, M.J.B., Clare, M.A., Sumner, E.J., Vendettuoli, D., Hughes Clarke, J.E., Hubbard, S.M., Talling, P.J., Lintern, D.G., Stacey, C.D., Englert, R.G., Vardy, M.E., Hunt, J.E., Yokokawa, M., Parsons, D.R., Hizzett, J.L., Azpiroz-Zabala, M., Vellinga, A.J., 2018. How to recognize crescentic bedforms formed by supercritical turbidity currents in the geologic record: Insights from active submarine channels. *Geology*, 46, 563–566.
- Harms, J.C., 1979. Primary sedimentary structures. *Annual Review of Earth and Planetary Sciences*, 7, 227–248.
- Hendershot, M.L., Venditti, J.G., Bradley, R.W., Kostaschuk, R.A., Church, M., Allison, M.A., 2016. Response of low-angle dunes to variable flow. *Sedimentology*, 63, 743–760.
- Holmes, R.R.J., Garcia, M.H., 2008. Flow over bedforms in a large sand-bed river: A field investigation. *Journal of Hydraulic Research*, 46, 322–333.

- Hosseini, S., Shamsai, A., Ataie-Ashtiani, B., 2006. Synchronous measurements of the velocity and concentration in low density turbidity currents using an Acoustic Doppler Velocimeter. *Flow Measurement and Instrumentation*, 17, 59–68.
- Huang, H., Imran, J., Pirmez, C., Zhang, Q., Chen, G., 2009. The critical densimetric Froude number of subaqueous gravity currents can be non-unity or non-existent. *Journal of Sedimentary Research*, 79, 479.
- Hughes Clarke, J.E., 2016. First wide-angle view of channelized turbidity currents links migrating cyclic steps to flow characteristics. *Nature communications*, 7, 11896.
- Iseya, F., 1984. An experimental study of dune development and its effect on sediment suspension. *Environmental Research Center papers*, 5, 1–56.
- Jopling, A.V., Forbes, D.L., 1979. Flume study of silt transportation and deposition. *Geografiska Annaler. Series A, Physical Geography*, 61, 67–85.
- Jorissen, A.L., 1938. Étude expérimentale du transport solide des cours d'eau. *Revue Universelle des Mines*, 14, 269–282.
- Julien, P.Y., 1992. *Study of bedform geometry in large rivers*. Technical Report Q1386, Delft Hydraulics, Emmeloord, Netherlands.
- Julien, P.Y., 2000. *Bed resistance to flow of the Bovenrijn-Waal rivers during the 1998 flood*. Technical Report Q2691, Delft Hydraulics, Delft, Netherlands.
- Julien, P.Y., Raslan, Y., 1998. Upper-regime plane bed. *Journal of Hydraulic Engineering*, 124, 1086–1096.
- Kalinske, A.A., Hsia, C.H., 1945. Study of transportation of fine sediments by flowing water.
- Kane, I.A., Clare, M.A., 2019. Dispersion, accumulation, and the ultimate fate of microplastics in deep-marine environments: A review and future directions. *Frontiers in*

- Earth Science*, 7, 80.
- Kennedy, J.F., 1961. *Stationary waves and antidunes in alluvial channels*. Technical Report KH-R-2, W.M. Keck Laboratory of Hydraulics and Water Resources, California Institute of Technology, Pasadena, CA.
- Kennedy, J.F., 1963. The mechanics of dunes and antidunes in erodible-bed channels. *Journal of Fluid Mechanics*, 16, 521–544.
- Keulegan, G.H., 1938. Laws of turbulent flow in open channels. *Journal National Bureau of Standards, Research Paper 1151*, 21, 707–741.
- Kneller, B.C., Bennett, S.J., McCaffrey, W.D., 1999. Velocity structure, turbulence and fluid stresses in experimental gravity currents. *Journal of Geophysical Research: Oceans*, 104, 5381–5391.
- Koller, D., Manica, R., Borges, A.d.O., Fedele, J., 2019. Experimental bedforms by saline density currents. *Brazilian Journal of Geology*, 49.
- Koller, D.K., 2016. *Estudo experimental de formas de fundo por correntes de densidade salina em canal de fundo móvel*. Master's thesis, Instituto de Pesquisas Hidraulicas, Universidade Federal do Rio Grande do Sul, Porto Alegre, Brazil.
- Koller, D.K., Borges, A.L.d.O., Puhl, E., Manica, R., 2017. Prediction of the bedforms generated by density currents based on fluvial phase diagrams. *RBRH*, 22.
- Kuhnle, R.A., Wren, D.G., 2009. Size of suspended sediment over dunes. *Journal of Geophysical Research: Earth Surface*, 114.
- Lancaster, N., 1988. The development of large aeolian bedforms. *Sedimentary Geology*, 55, 69–89.
- Lapotre, M.G.A., Lamb, M.P., McElroy, B., 2017. What sets the size of current ripples? *Geology*, 45, 243–246.

- Laursen, E.M., 1958. The total sediment load of streams. *Journal of the Hydraulics Division*, 84, 1–36.
- Leclair, S.F., 2002. Preservation of cross-strata due to the migration of subaqueous dunes: an experimental investigation. *Sedimentology*, 49, 1157–1180.
- Lesshafft, L., Meiburg, E., Kneller, B., Marsden, A., 2011. Towards inverse modeling of turbidity currents: The inverse lock-exchange problem. *Computers & Geosciences*, 37, 521–529.
- Liu, J.T., Wang, Y.H., Yang, R.J., Hsu, R.T., Kao, S.J., Lin, H.L., Kuo, F.H., 2012. Cyclone-induced hyperpycnal turbidity currents in a submarine canyon. *Journal of Geophysical Research: Oceans*, 117, C04033.
- Lowe, D.R., 1988. Suspended-load fallout rate as an independent variable in the analysis of current structures. *Sedimentology*, 35, 765–776.
- Luchi, R., Balachandar, S., Seminara, G., Parker, G., 2018. Turbidity currents with equilibrium basal driving layers: A mechanism for long runout. *Geophysical Research Letters*, 45, 1518–1526.
- Mahmood, K., Tarar, R.N., Hassan, S., Khan, H., Masood, T., 1979. Selected equilibrium-state data from ACOP canals. *Rep. No. EWR-79-2*.
- Mahmoudi, N., Duman, E., 2015. Detecting credit card fraud by Modified Fisher Discriminant Analysis. *Expert Systems with Applications*, 42, 2510–2516.
- Meyer-Peter, E., Müller, R., 1948. Formulas for bed-load transport, in: *Proceedings of the 2nd Meeting of the International Association of Hydraulic Research*, IAHR, Stockholm, Sweden, pp. 39–64.
- Mezaki, S., 1973. Bed forms in the Yoro river at Azu, Chiba prefecture [in Japanese]. *Geographical Review of Japan*, 46, 516–532.

- Mutter, D.G., 1971. *A Flume Study of Alluvial Bed Configurations*. Master's thesis, Faculty of Graduate Studies, University of Alberta, Edmonton, Alberta, Canada.
- Naqshband, S., Ribberink, J.S., Hurther, D., Hulscher, S.J.M.H., 2014. Bed load and suspended load contributions to migrating sand dunes in equilibrium. *Journal of Geophysical Research: Earth Surface*, 119, 1043–1063.
- Naruse, H., Nakao, K., 2021. Inverse modeling of turbidity currents using an artificial neural network approach: verification for field application. *Earth Surface Dynamics*, 9, 1091–1109.
- Neill, C.R., 1969. Bed forms in the Lower Red Deer River, Alberta. *Journal of Hydrology*, 7, 58–85.
- Nezu, I., Rodi, W., 1986. Open-channel flow measurements with a laser doppler anemometer. *Journal of Hydraulic Engineering*, 112, 335–355.
- Nomicos, G.N., 1956. *Effects of sediment load on the velocity field and friction factor of turbulent flow in an open channel*. Ph.D. thesis, California Institute of Technology, Pasadena, California.
- Nordin, C.F., 1976. Flume studies with fine and coarse sands. *Open File Rep. No. 76–762*.
- Normark, W.R., Piper, D.J., Posamentier, H., Pirmez, C., Migeon, S., 2002. Variability in form and growth of sediment waves on turbidite channel levees. *Marine Geology*, 192, 23–58.
- Ohata, K., Naruse, H. & Izumi, N., 2022. Upper and lower plane bed definitions revised. *Progress in Earth and Planetary Science*, 9, 23.
- Ohata, K., Naruse, H., Yokokawa, M., Viparelli, E., 2017. New bedform phase diagrams and discriminant functions for formative conditions of bedforms in open-channel flows. *Journal of Geophysical Research: Earth Surface*, 122, 2139–2158.

- Onishi, Y., Jain, S.C., Kennedy, J.F., 1976. Effects of meandering in alluvial streams. *Journal of the Hydraulics Division*, 102, 899–918.
- Owens, J.S., 1908. Experiments on the transporting power of sea currents. *The Geographical Journal*, 31, 415–420.
- Parker, G., Fukushima, Y., Pantin, H.M., 1986. Self-accelerating turbidity currents. *Journal of Fluid Mechanics*, 171, 145–181.
- Parkinson, S.D., Funke, S.W., Hill, J., Piggott, M.D., Allison, P.A., 2017. Application of the adjoint approach to optimise the initial conditions of a turbidity current with the AdjointTurbidity 1.0 model. *Geoscientific Model Development*, 10, 1051–1068.
- Paull, C.K., Talling, P.J., Maier, K.L., Parsons, D., Xu, J., Caress, D.W., Gwiazda, R., Lundsten, E.M., Anderson, K., Barry, J.P., Chaffey, M., O'Reilly, T., Rosenberger, K.J., Gales, J.A., Kieft, B., McGann, M., Simmons, S.M., McCann, M., Sumner, E.J., Clare, M.A., Cartigny, M.J., 2018. Powerful turbidity currents driven by dense basal layers. *Nature Communications*, 9, 4114.
- Pitlick, J., 1992. Flow resistance under conditions of intense gravel transport. *Water Resources Research*, 28, 891–903.
- Pratt, C.J., 1970. *Summary of experimental data for flume tests over 0.49 mm sand*. Technical Report, Department of Civil Engineering, University of Southampton, Southampton, England.
- Rathbun, R.E., Guy, H.P., 1967. Measurement of hydraulic and sediment transport variables in a small recirculating flume. *Water Resources Research*, 3, 107–122.
- Recking, A., Bacchi, V., Naaim, M., Frey, P., 2009. Antidunes on steep slopes. *Journal of Geophysical Research: Earth Surface*, 114.
- Sequeiros, O.E., Spinewine, B., Beaubouef, R.T., Sun, T., García, M.H., Parker, G., 2010a.

- Bedload transport and bed resistance associated with density and turbidity currents. *Sedimentology*, 57, 1463–1490.
- Sequeiros, O.E., Spinewine, B., Beaubouef, R.T., Sun, T., García, M.H., Parker, G., 2010b. Characteristics of velocity and excess density profiles of saline underflows and turbidity currents flowing over a mobile bed. *Journal of Hydraulic Engineering*, 136, 412–433.
- Shaw, J., Kellerhals, R., 1977. Paleohydraulic interpretation of antidune bedforms with applications to antidunes in gravel. *Journal of Sedimentary Research*, 47, 257–266.
- Shen, H.W., Harrison, A.S., Mellema, W.J., 1978. Temperature and Missouri river stages near Omaha. *Journal of the Hydraulics Division*, 104, 1–20.
- Shields, A., 1936. *Application of similarity principles and turbulence research to bed-load movement (English translation of an original German manuscript)*. Technical Report 167, Soil Conservation Service Cooperative Laboratory, California Institute of Technology, Pasadena, CA.
- Shinohara, K., Tsubaki, T., 1959. On the characteristics of sand waves formed upon beds of the open channels and rivers. *Report of Research Institute for Applied Mechanics*, VII.
- Simons, D.B., 1957. *Theory and design of stable channels in alluvial material*. Ph.D. thesis, Colorado State University, Fort Collins, Colorado.
- Simons, D.B., Richardson, E.V., 1966. *Resistance to flow in alluvial channels*. Technical Report Professional Paper 422-J, U. S. Geological Survey, Washington, DC.
- Singh, B., 1960. *Transport of bed-load in channels with special reference to gradient and form*. Ph.D. thesis, University of London, London, England.
- Southard, J.B., Boguchwal, L.A., 1990. Bed configurations in steady unidirectional water flows. Part 2. Synthesis of flume data. *Journal of Sedimentary Petrology*, 60, 658–679.

- Stein, R.A., 1965. Laboratory studies of total load and apparent bed load. *Journal of Geophysical Research*, 70, 1831–1842.
- Straub, L.G., 1954. Transportation characteristics Missouri river sediment. *M.R.D. Sediment Series No. 4*.
- Straub, L.G., Anderson, A.G., Flammer, G.H., 1958. Experiments on the influence of temperature on the sediment load. *M.R.D. Sediment Series No. 10*.
- Sukhodolov, A.N., Fedele, J.J., Rhoads, B.L., 2006. Structure of flow over alluvial bedforms: an experiment on linking field and laboratory methods. *Earth Surface Processes and Landforms*, 31, 1292–1310.
- Taki, K., Parker, G., 2005. Transportational cyclic steps created by flow over an erodible bed. part 1. experiments. *Journal of Hydraulic Research*, 43, 488–501.
- Tanaka, Y., 1970. An experimental study on anti-dunes. *Disaster Prevention Research Institute Annuals*, 13, 271–284.
- Taylor, B.D., 1971. *Temperature effects in alluvial streams*. Technical Report KH-R-27, W. M. Keck Laboratory of Hydraulics and Water Resources, California Institute of Technology, Pasadena, CA.
- Telfer, M.W., Parteli, E.J.R., Radebaugh, J., Beyer, R.A., Bertrand, T., Forget, F., Nimmo, F., Grundy, W.M., Moore, J.M., Stern, S.A., Spencer, J., Lauer, T.R., Earle, A.M., Binzel, R.P., Weaver, H.A., Olkin, C.B., Young, L.A., Ennico, K., Runyon, K., 2018. Dunes on Pluto. *Science*, 360, 992–997.
- Termes, A.P.P., 1986. *Dimensies van beddingvormen onder permanente stromingsomstandigheden bij hoog sedimenttransport [in Dutch]*. Technical Report M2130, Verslag Onderzoek.
- Tsubaki, T., Kawasumi, T., Yasutomi, T., 1953. On the influences of sand ripples upon the

- sediment transport in open channels. *Report of Research Institute for Applied Mechanics, II*.
- Tubau, X., Paull, C.K., Lastras, G., Caress, D.W., Canals, M., Lundsten, E., Anderson, K., Gwiazda, R., Amblas, D., 2015. Submarine canyons of Santa Monica Bay, Southern California: Variability in morphology and sedimentary processes. *Marine Geology*, 365, 61–79.
- Ueno, T., 1981. On the regions of occurrence of ripples and dunes (in Japanese). *Proceedings of the Japanese Conference on Hydraulics*, 25, 93–98.
- United States Army Corps of Engineers, U.S. Waterways Experiment Station, Vicksburg, Mississippi, 1935. Studies of river bed materials and their movement with special reference to the lower Mississippi River, paper 17, 161 pp.
- van den Berg, J.H., van Gelder, A., 1993. A new bedform stability diagram, with emphasis on the transition of ripples to plane bed in flows over fine sand and silt, in: Marzo, M., Puigdefabregas, C. (Eds.), *Alluvial sedimentation*, Blackwell Scientific Publications, volume 17, pp. 11–21.
- Vanoni, V.A., 1974. Factors determining bed forms of alluvial streams. *Journal of the Hydraulics Division*, 100, 363–377.
- Vanoni, V.A., Brooks, N.H., 1957. *Laboratory studies of the roughness and suspended load of alluvial streams*. Technical Report E-68, W. M. Keck Laboratory of Hydraulics and Water Resources, California Institute of Technology, Pasadena, CA.
- Vanoni, V.A., Hwang, L.S., 1967. Bed forms and friction in streams. *Journal of the Hydraulics Division*, 93, 121–144.
- Vendettuoli, D., Clare, M.A., Hughes Clarke, J.E., Vellinga, A., Hizzet, J., Hage, S., Cartigny, M.J.B., Talling, P.J., Waltham, D., Hubbard, S.M., Stacey, C., Lintern, D.G., 2019. Daily bathymetric surveys document how stratigraphy is built and its extreme

- incompleteness in submarine channels. *Earth and Planetary Science Letters*, 515, 231–247.
- Venditti, J.G., Bauer, B.O., 2005. Turbulent flow over a dune: Green River, Colorado. *Earth Surface Processes and Landforms*, 30, 289–304.
- Venditti, J.G., Church, M., Bennett, S.J., 2005. On the transition between 2d and 3d dunes. *Sedimentology*, 52, 1343–1359.
- Waltham, D., 2004. Flow transformations in particulate gravity currents. *Journal of Sedimentary Research*, 74, 129–134.
- Wijbenga, J.H.A., Klaassen, G.J., 1983. Changes in bedform dimensions under unsteady flow conditions in a straight flume, in: *Modern and Ancient Fluvial Systems*, edited by Collinson, J. D. and Lewin, J., Blackwell Publishing Ltd., pp. 35–48.
- Wilbers, A., 2004. *The development and hydraulic roughness of subaqueous dunes*. Ph.D. thesis, Utrecht University, Utrecht, Netherlands.
- Williams, G.P., 1970. *Flume width and water depth effects in sediment transport experiments*. United States Government Printing Office, Washington, DC.
- Willis, J.C., Coleman, N.L., Ellis, W.M., 1972. Laboratory study of transport of fine sand. *Journal of the Hydraulics Division*, 98, 489–501.
- Wong, M., Parker, G., 2006. Reanalysis and correction of bed-load relation of Meyer-Peter and Müller using their own database. *Journal of Hydraulic Engineering*, 132, 1159–1168.
- Wren, D.G., Kuhnle, R.A., Wilson, C.G., 2007. Measurements of the relationship between turbulence and sediment in suspension over mobile sand dunes in a laboratory flume. *Journal of Geophysical Research: Earth Surface*, 112.
- Wu, Y., Lu, Y., Sun, H., Huang, H., 2019. Checking dilute subaqueous density flows from the specific energy diagram. *Journal of Hydraulic Research*, 0, 1–6.
- Xu, J.P., 2010. Normalized velocity profiles of field-measured turbidity currents. *Geology*,

38, 563–566.

Yokokawa, M., Hasegawa, K., Kanbayashi, S., Endo, N., 2010. Formative conditions and sedimentary structures of sandy 3d antidunes: an application of the gravel step-pool model to fine-grained sand in an experimental flume. *Earth Surface Processes and Landforms*, 35, 1720–1729.

Znamenskaya, N.S., 1963. Experimental study of the dune movement of sediment, in: *Soviet Hydrology: Selected Papers*, American Geophysical Union, Washington, DC, pp. 253–275.

Zou, M., Sun, C., Liang, S., Sun, Y., Li, D., Li, L., Fan, L., Wu, L., Xia, W., 2019. Fisher discriminant analysis for classification of autism spectrum disorders based on folate-related metabolism markers. *The Journal of Nutritional Biochemistry*, 64, 25–31.

FIGURE CAPTIONS

Figure 1 | Typical vertical profiles of (A) velocity of open-channel flows, (B) velocity of gravity currents, and (C) density of gravity currents. (A) V – mean flow velocity, h – flow depth. (B) U – layer-averaged flow velocity, U_m – maximum flow velocity, H – layer-averaged flow thickness, H_m – the height showing the maximum velocity, H_a – the height of interface between gravity current and ambient fluid. (C) ρ_g – mean density of whole layer, ρ_{gl} – mean density of lower layer, ρ_a – density of ambient water.

Figure 2 | Sketch of the experimental facility.

Figure 3 | Grain-size distributions of plastic particles.

Figure 4 | Velocity and density profiles of Run 7.

Figure 5 | Velocity profile of Run 7 and fitted curves to the data within $0.01 \text{ m} < z < 0.02 \text{ m}$.

Figure 6 | Comparison of H_m/H of the experimental data by Koller (2016) with the empirical relationship (Equation 9) proposed by Abad *et al.* (2011). The ratio H_m/H for Fedele *et al.* (2016) was estimated using the Abad's relationship.

Figure 7 | Comparison of R_b or the data of Koller (2016) between that calculated using the density profile and that estimated using the empirical relationships (Eqs 9 and 13–

15) proposed by Abad *et al.* (2011). (A) plastic particles. (B) natural sands.

Figure 8 | Comparison between data of gravity-current bedforms by Koller (2016) with the scaling relation (Eq. 32).

Figure 9 | Snapshots of Run 7 ($Q_{in} = 1.5$ L/s, $S = 0.7$ degrees, and $D_{50} = 428.3$ μm).

Figure 10 | Snapshots of Run 9 ($Q_{in} = 2$ L/s, $S = 0.7$ degrees, and $D_{50} = 428.3$ μm).

Figure 11 | Comparison between data of gravity-current bedforms obtained by this study with the scaling relation (Eq. 32).

Figure 12 | Snapshots of Run 3 ($Q_{in} = 1.5$ L/s, $S = 3$ degrees, and $D_{50} = 428.3$ μm).

Figure 13 | Snapshots of Run 5 ($Q_{in} = 2$ L/s, $S = 3$ degrees, and $D_{50} = 253.5$ μm).

Figure 14 | Shields number versus particle Reynolds number.

Figure 15 | Froude number versus particle Reynolds number.

Figure 16 | Velocity-depth diagrams of bedforms for finer sediment ($Re_p, Re_{pg} \leq 11.37$). (A) Dimensionless flow thickness H^0 versus dimensionless flow velocity U^0 . (B) Dimensionless flow thickness of lower layer H_m^0 versus dimensionless maximum flow velocity U_m^0 .

Figure 17 | Velocity-depth diagrams of bedforms for coarser sediment ($Re_p, Re_{pg} > 11.37$). (A) Dimensionless flow thickness H^0 versus dimensionless flow velocity U^0 . (B) Dimensionless flow thickness of lower layer H_m^0 versus dimensionless maximum flow velocity U_m^0 .

Figure 18 | Comparison of phase spaces of density-current bedforms with phase spaces of open-channel flow bedforms ($Re_p, Re_{pg} \leq 11.37$) obtained by the discriminant analysis. (A) Dimensionless flow thickness H^0 versus dimensionless flow velocity U^0 . (B) Dimensionless flow thickness of lower layer H_m^0 versus dimensionless maximum flow velocity U_m^0 .

Figure 19 | Comparison of phase spaces of density-current bedforms with phase spaces of open-channel flow bedforms ($Re_p, Re_{pg} > 11.37$) obtained by the discriminant analysis. (A) Dimensionless flow thickness H^0 versus dimensionless flow velocity U^0 . (B) Dimensionless flow thickness of lower layer H_m^0 versus dimensionless maximum flow velocity U_m^0 .

Table 1 | Characteristics of sediments.

Sediment	ρ_s [kg/m ³]	D_{10} [μm]	D_{30} [μm]	D_{50} [μm]	D_{70} [μm]	D_{90} [μm]	σ_g [kg/m ³]
1	1500	168.6	214.2	253.6	299.9	382.2	1.375
2	1500	283.6	360.8	428.3	509.5	657.9	1.384

Table 2 | Experimental conditions and results.

Run	S [deg]	D_{50} [μm]	Q_{in} [L/s]	U [m/s]	H [m]	u_* [m/s]	ρ_g [kg/m ³]	U_m [m/s]	H_m [m]	ρ_{gL} [kg/m ³]	Duration [min]	λ [cm]	Bedform
3	3.0	428	1.5	0.4	0.15	0.032	1014.7	0.52	0.044	1031.0	40	60 <	Antidune
5	3.0	253.5	2.0	0.5	0.21	0.035	1019.7	0.64	0.062	1036.7	30	100 <	Antidune
6	0.7	253.5	2.0	0.24	0.18	0.036	1036.7	0.31	0.054	1048.3	30	18.1	Ripple/dune
7	0.7	428	1.5	0.15	0.15	0.019	1027.6	0.19	0.044	1044.2	40	13.8	Ripple
9	0.7	428	2.0	0.19	0.17	0.014	1038	0.24	0.052	1048.5	30	15.9	Ripple/dune
10	0.7	428	3.0	0.19	0.18	0.037	1033.2	0.24	0.053	1042.9	15	14.4	Ripple/dune

Table 3| Error rates for open-channel flow bedforms. The parameter N denotes the total number of data points, n_e is the number of misclassified data points and r_e is the error rate.

Bedform	$Re_p \leq 11.37$			$Re_p > 11.37$		
	N	n_e	r_e	N	n_e	r_e
Ripple	67	10	0.15	119	1	0.01
Ripple/dune	146	12	0.08	396	15	0.04
Dune	65	3	0.05	377	48	0.13
Upper plane bed	132	25	0.19	127	42	0.33
Antidune	67	19	0.28	180	40	0.22
Total	477	69	0.14	1199	146	0.12

Table 4 | Error rates for gravity-current bedforms with $Re_p \leq 11.37$. The parameter N denotes the total number of data points, n_e is the number of misclassified data points and r_e is the error rate.

Bedform	N	Whole layer		Lower layer	
		n_e	r_e	n_e	r_e
Ripple	49	0	0.00	8	0.16
Dune	13	11	0.85	5	0.38
Upper plane bed	4	2	0.50	0	0.00
Antidune	24	24	1.00	23	0.96
Total	90	37	0.41	36	0.40

Table 5 | Error rates for gravity-current bedforms with $Re_p > 11.37$. The parameter N denotes the total number of data points, n_e is the number of misclassified data points and r_e is the error rate.

Bedform	N	Whole layer		Lower layer	
		n_e	r_e	n_e	r_e
Ripple	10	0	0.00	0	0.00
Dune	25	25	1.00	4	0.16
Antidune	7	7	1.00	6	0.86
Total	42	32	0.76	10	0.24

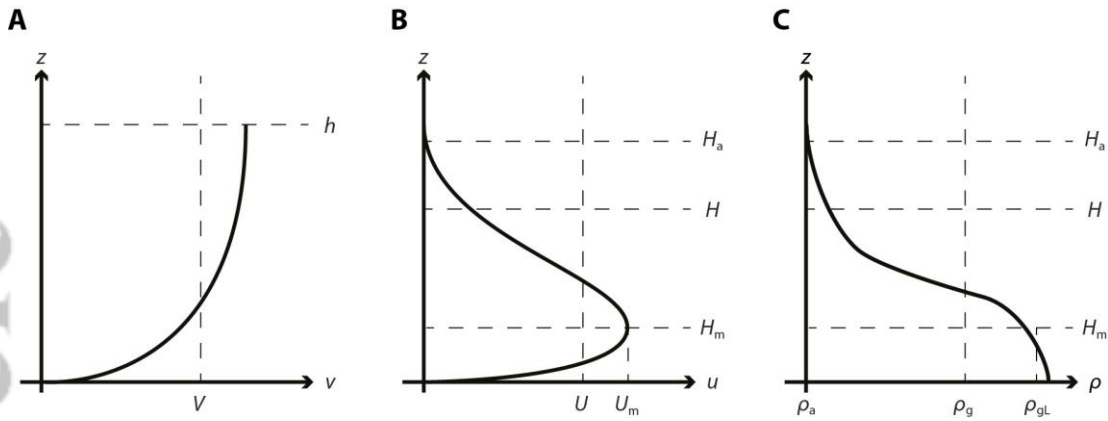


Figure 1 | Typical vertical profiles of (A) velocity of open-channel flows, (B) velocity of gravity currents, and (C) density of gravity currents. (A) V – mean flow velocity, h – flow depth. (B) U – layer-averaged flow velocity, U_m – maximum flow velocity, H – layer-averaged flow thickness, H_m – the height showing the maximum velocity, H_a – the height of interface between gravity current and ambient fluid. (C) ρ_g – mean density of whole layer, ρ_{gL} – mean density of lower layer, ρ_a – density of ambient water.

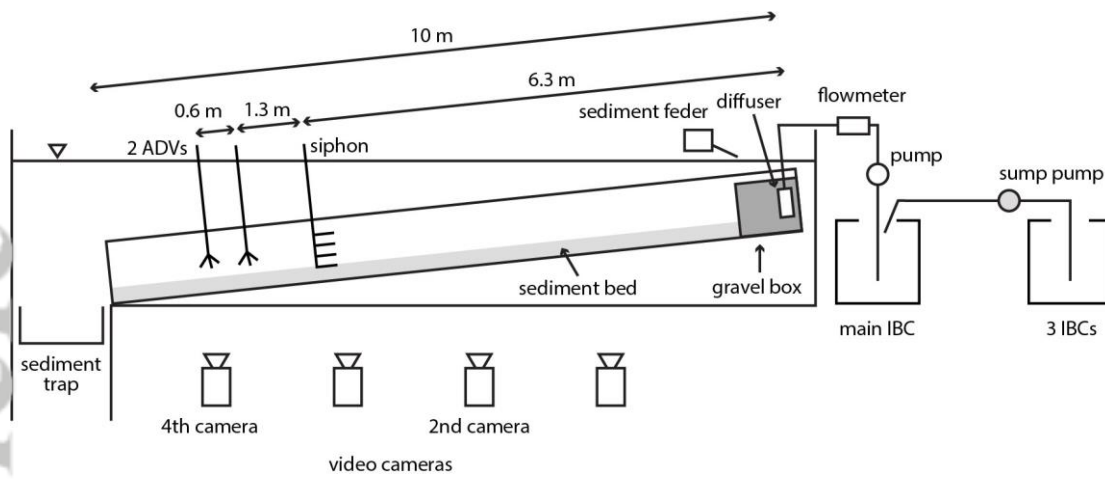


Figure 2 | Sketch of the experimental facility.

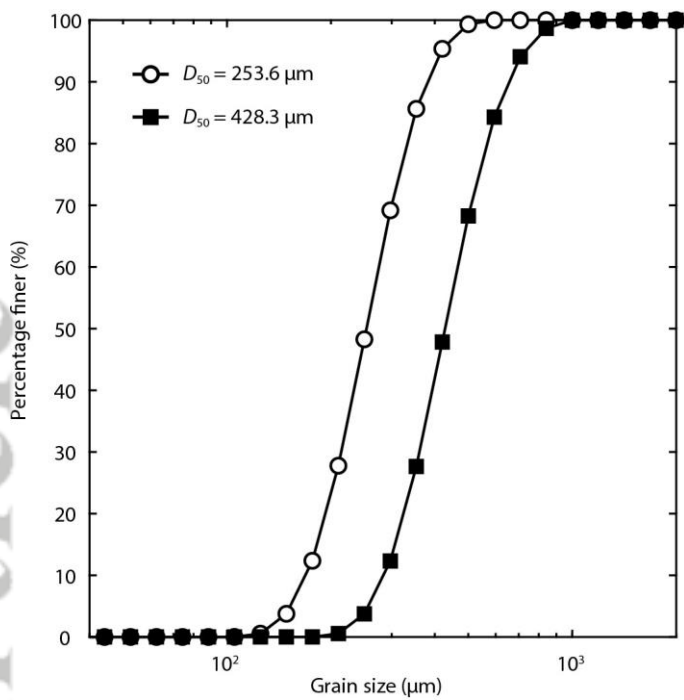


Figure 3 | Grain size distributions of plastic particles.

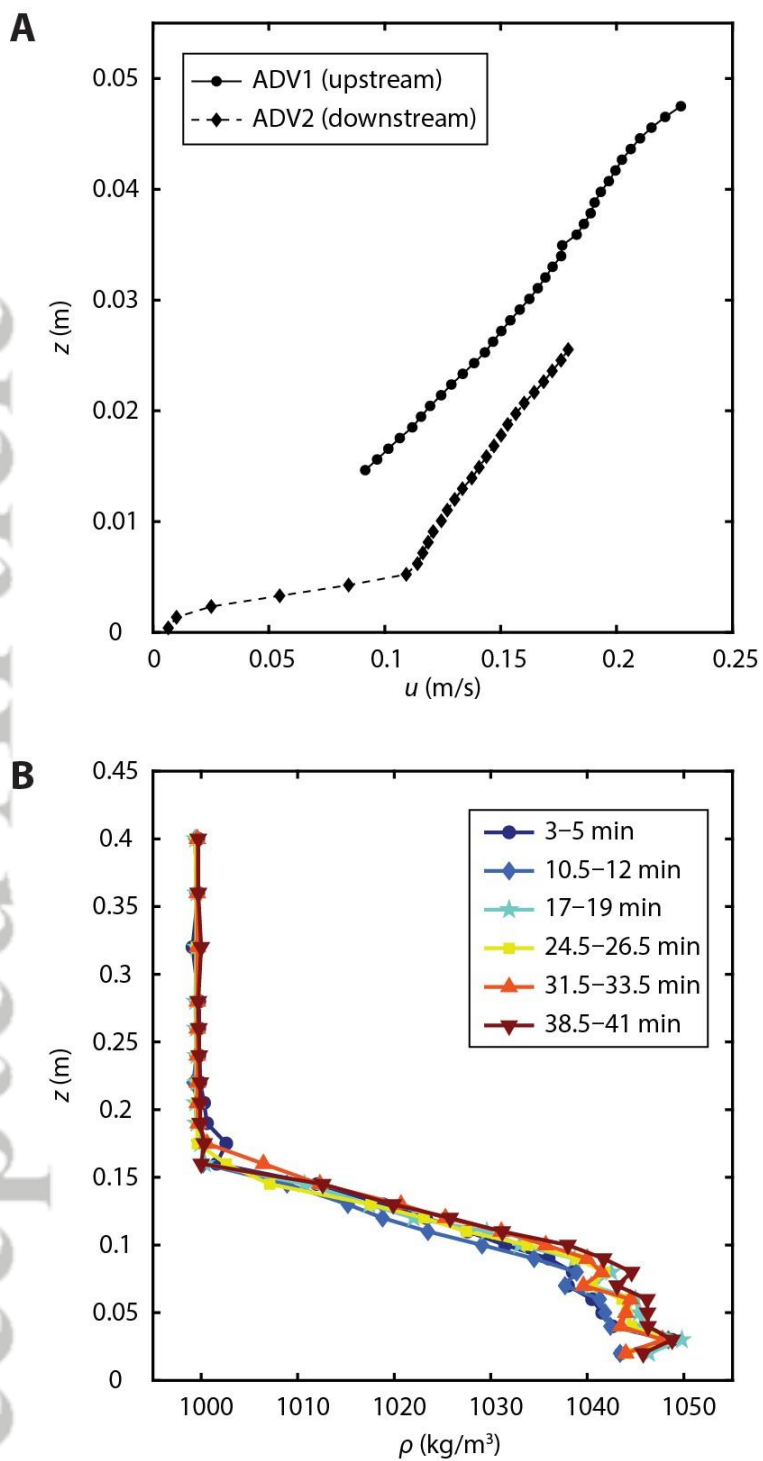


Figure 4 | Velocity and density profiles of Run 7.

Accepted Article

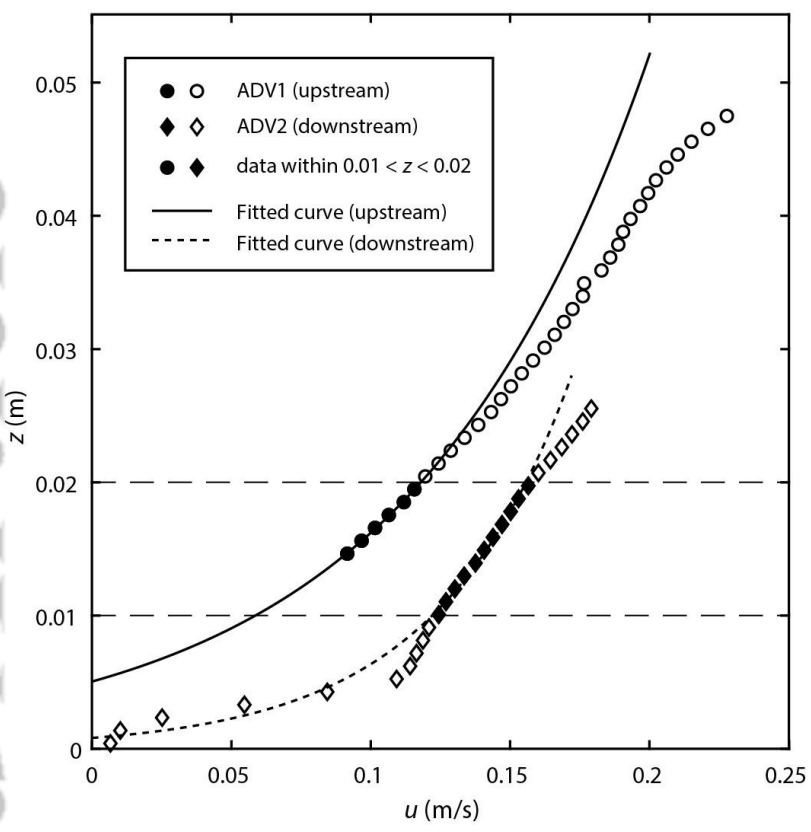


Figure 5 | Velocity profile of Run 7 and fitted curves to the data within $0.01 \text{ m} < z < 0.02$ m.

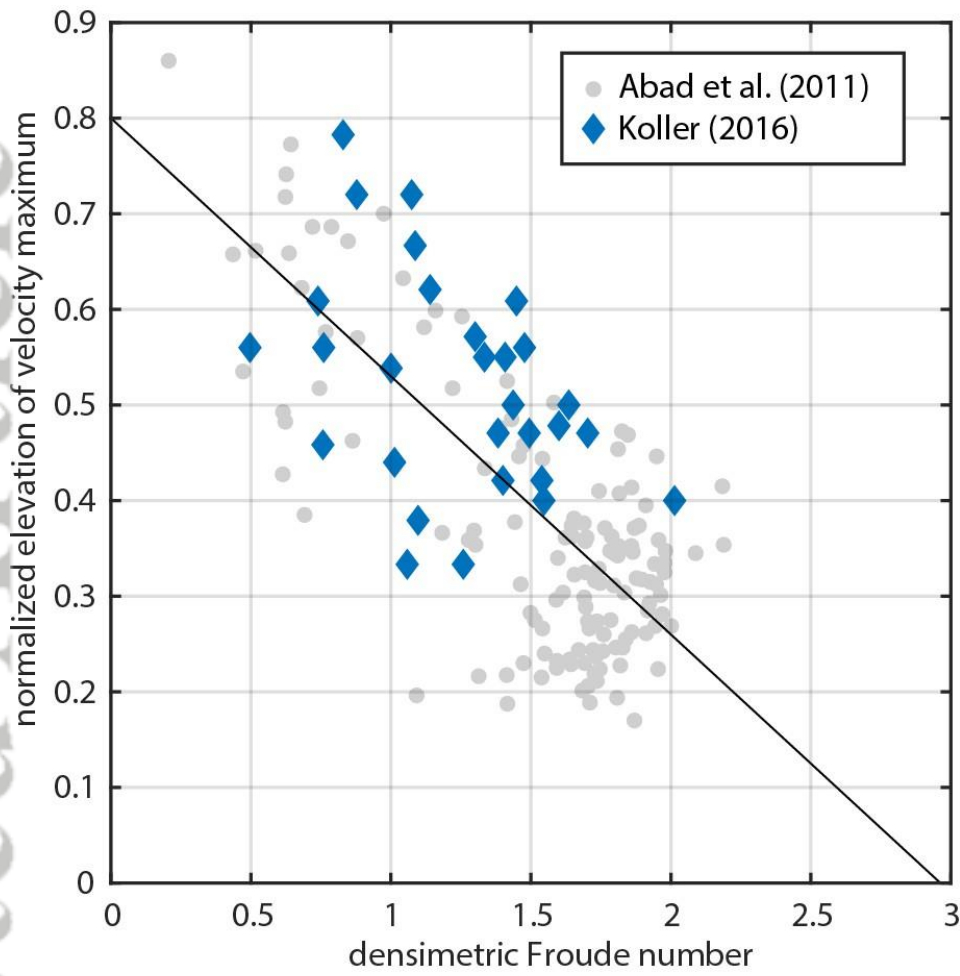


Figure 6 | Comparison of H_m/H of the experimental data by Koller [2016] with the empirical relationship (Equation 9) proposed by Abad et al. [2011]. The ratio H_m/H for Fedele et al. [2016] was estimated using the Abad’s relationship.

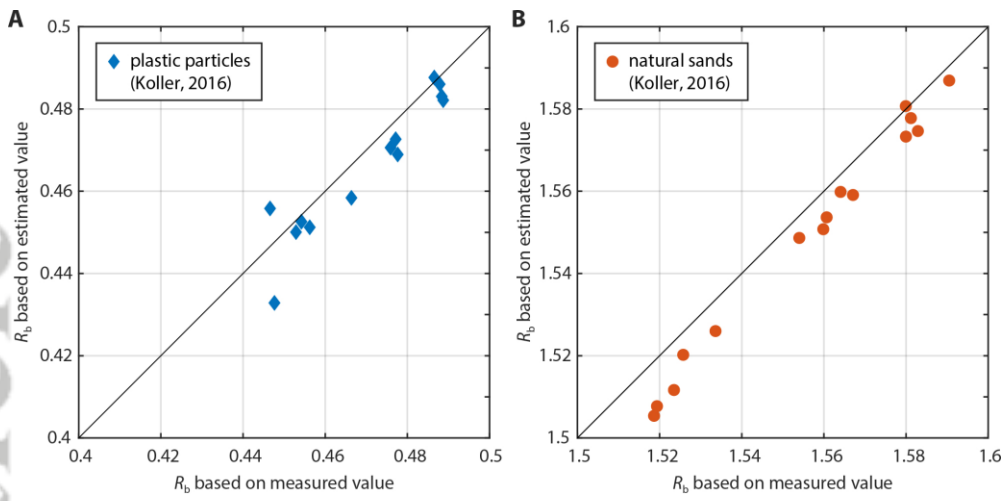


Figure 7 | Comparison of R_b or the data of Koller [2016] between that calculated using the density profile and that estimated using the empirical relationships (Equations 9 and 13–15) proposed by Abad et al. [2011]. (A) plastic particles. (B) natural sands.

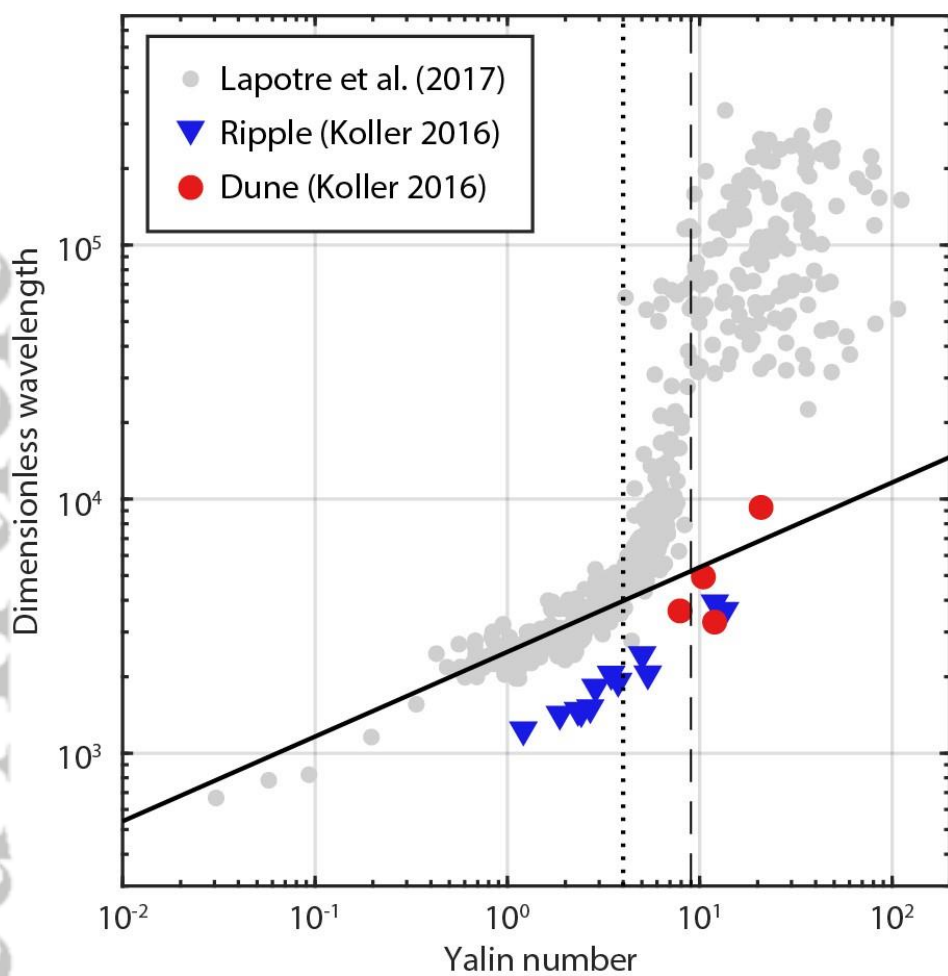


Figure 8 | Comparison between data of gravity-current bedforms by Koller [2016] with the scaling relation (Equation 32).

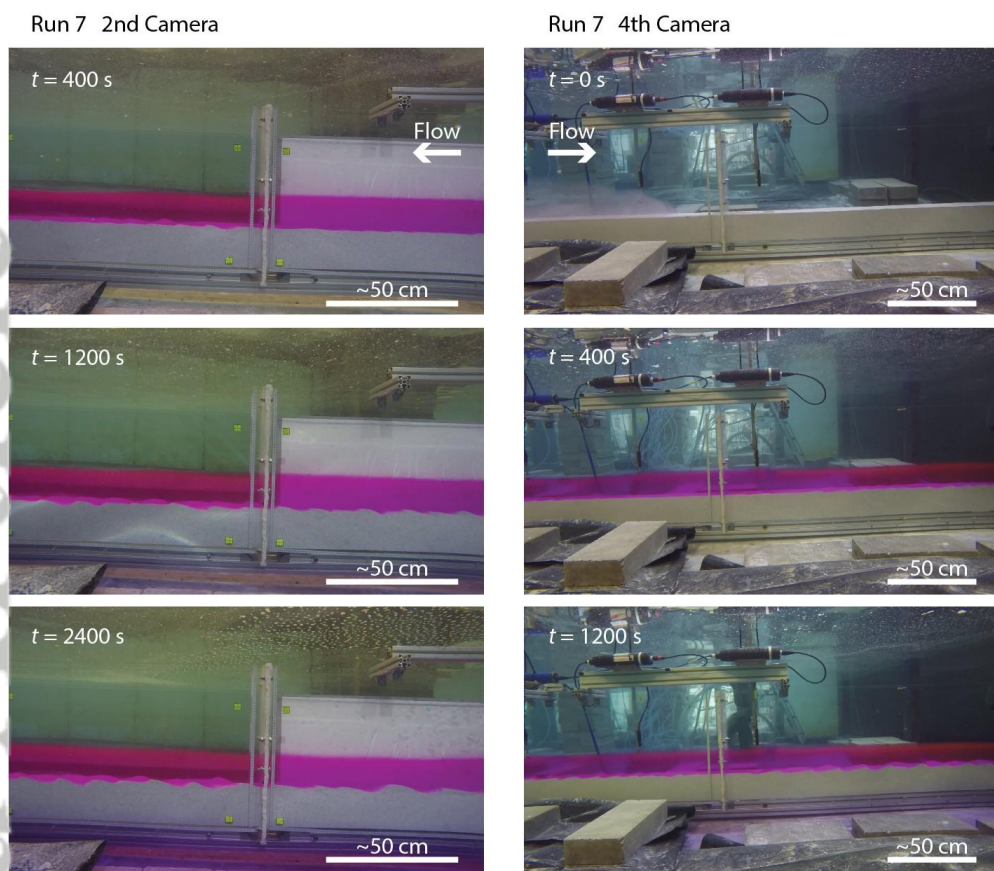


Figure 9 | Snapshots of Run 7 ($Q_{\text{in}} = 1.5 \text{ L/s}$, $S = 0.7$ degrees, and $D_{50} = 428.3 \mu\text{m}$).

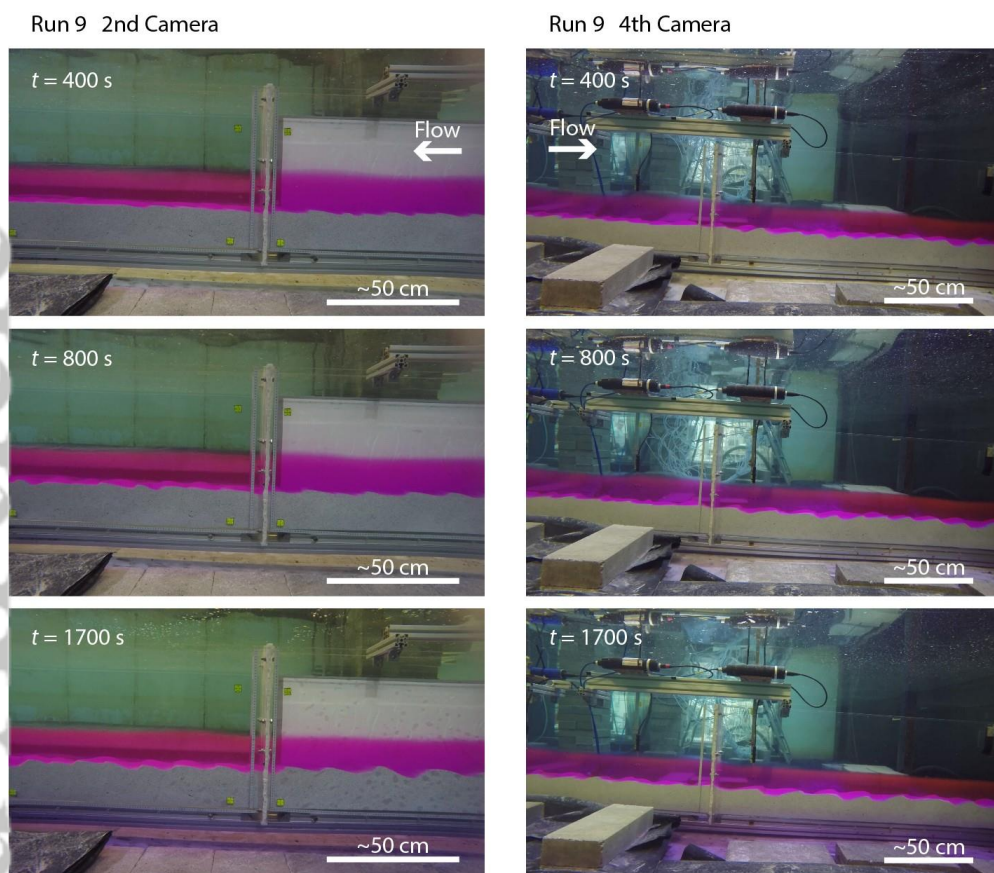


Figure 10 | Snapshots of Run 9 ($Q_{\text{in}} = 2 \text{ L/s}$, $S = 0.7$ degrees, and $D_{50} = 428.3 \mu\text{m}$).

Accepted Article

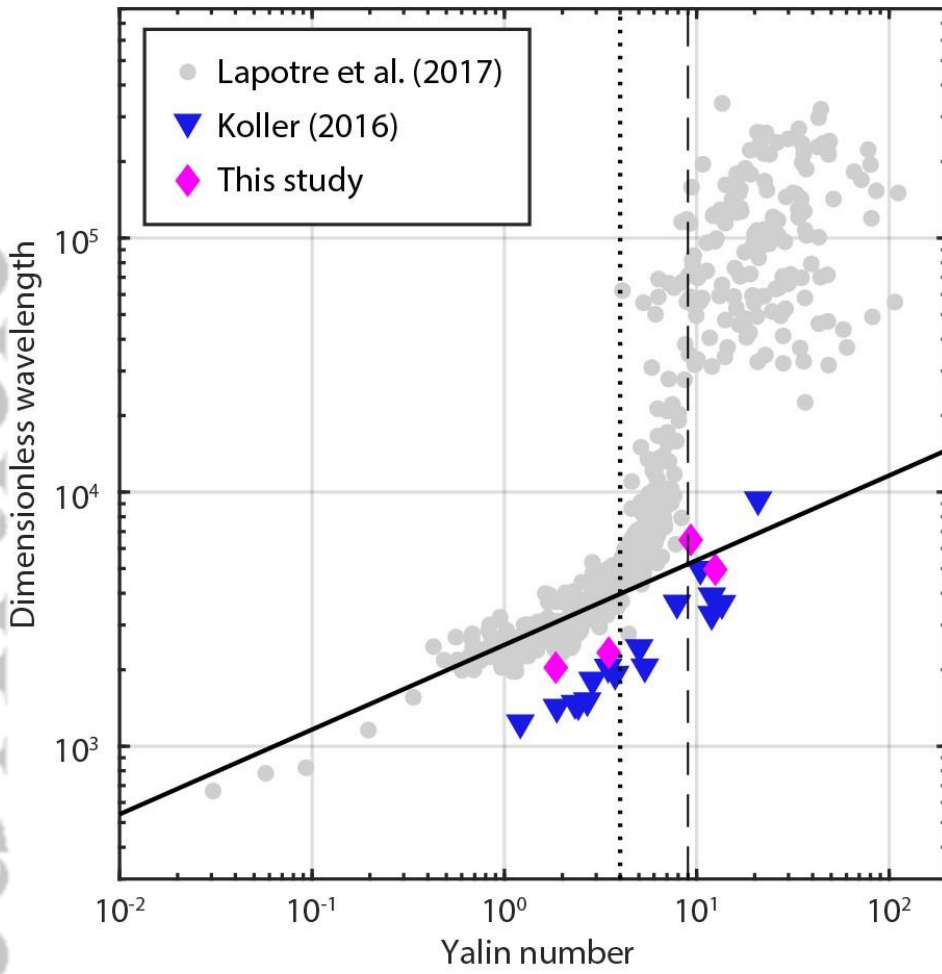


Figure 11 | Comparison between data of gravity-current bedforms obtained by this study with the scaling relation (Equation 32).

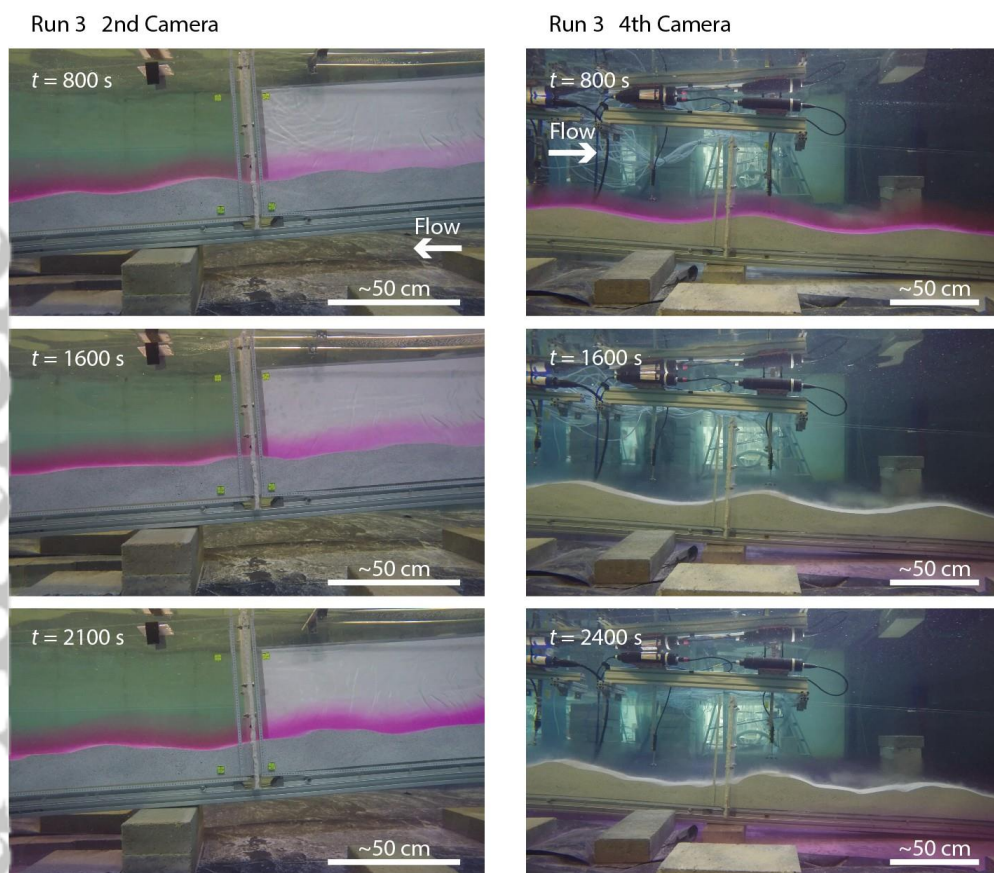


Figure 12 | Snapshots of Run 3 ($Q_{in} = 1.5$ L/s, $S = 3$ degrees, and $D_{50} = 428.3$ μ m).

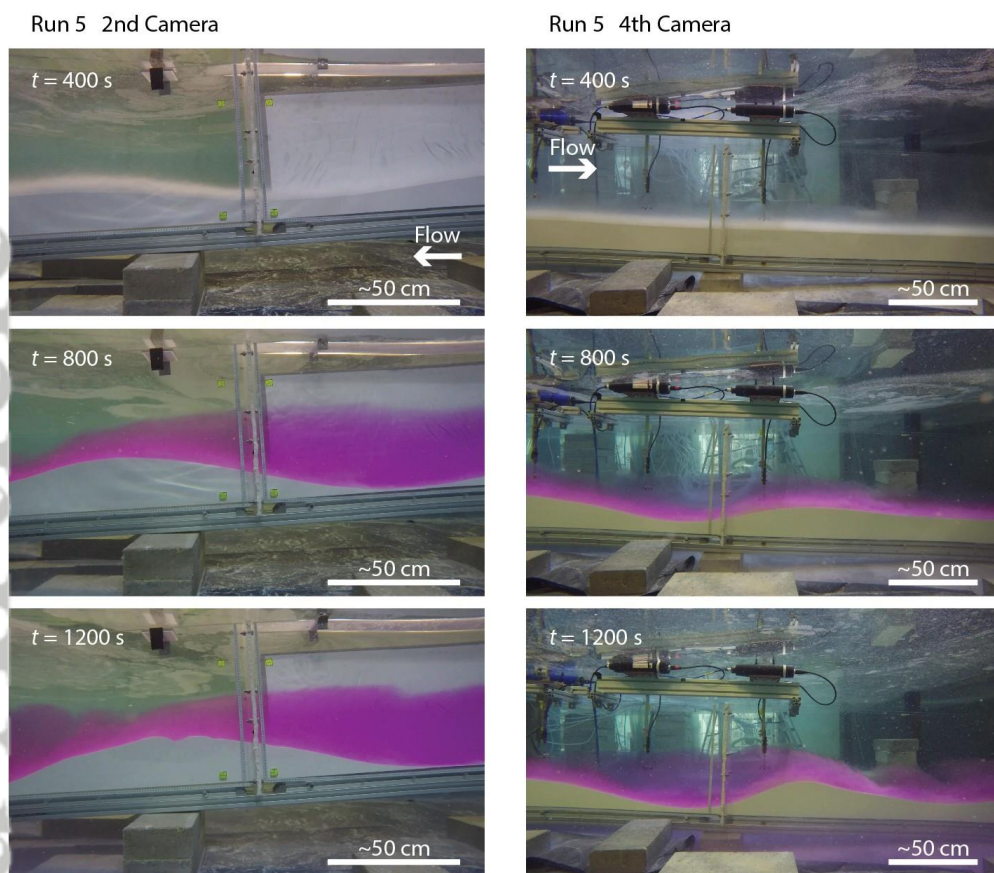


Figure 13 | Snapshots of Run 5 ($Q_{in} = 2 \text{ L/s}$, $S = 3 \text{ degrees}$, and $D_{50} = 253.5 \mu\text{m}$).

Accepted Article

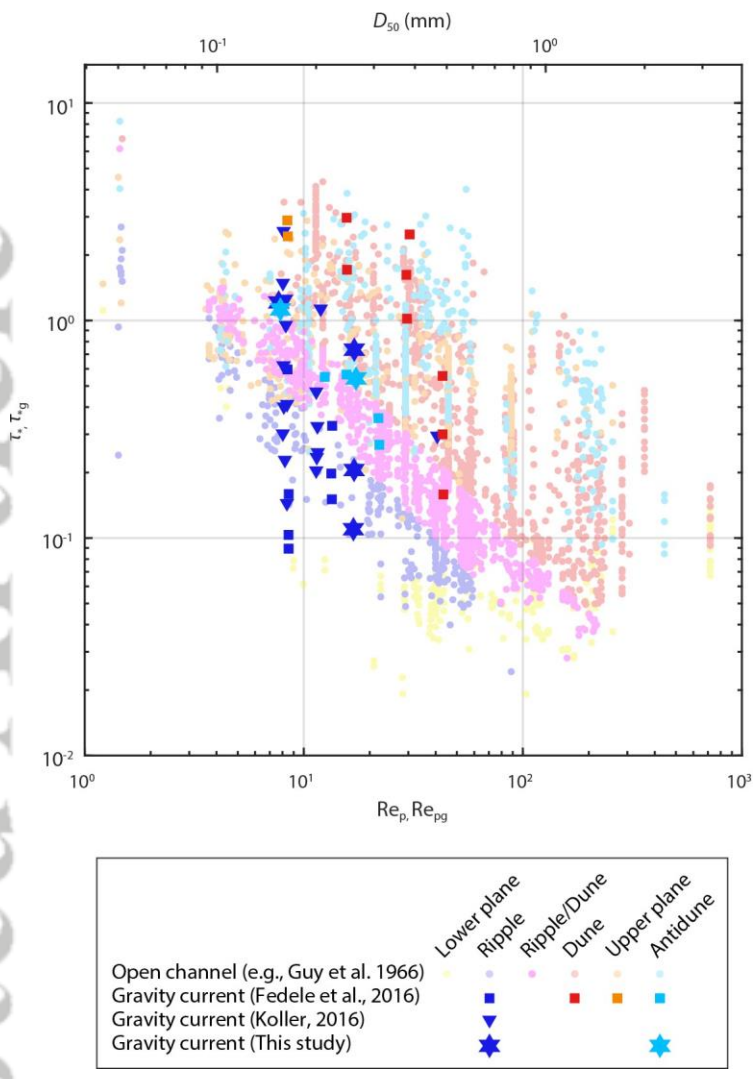


Figure 14 | Shields number versus particle Reynolds number.

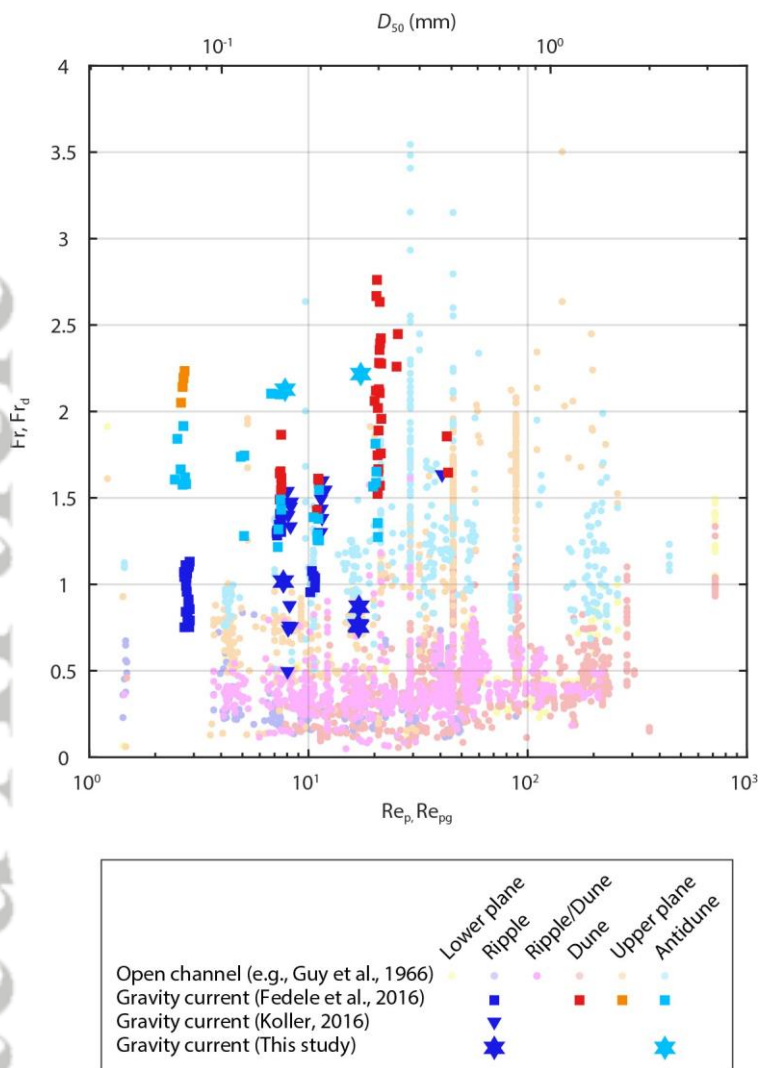


Figure 15 | Froude number versus particle Reynolds number.

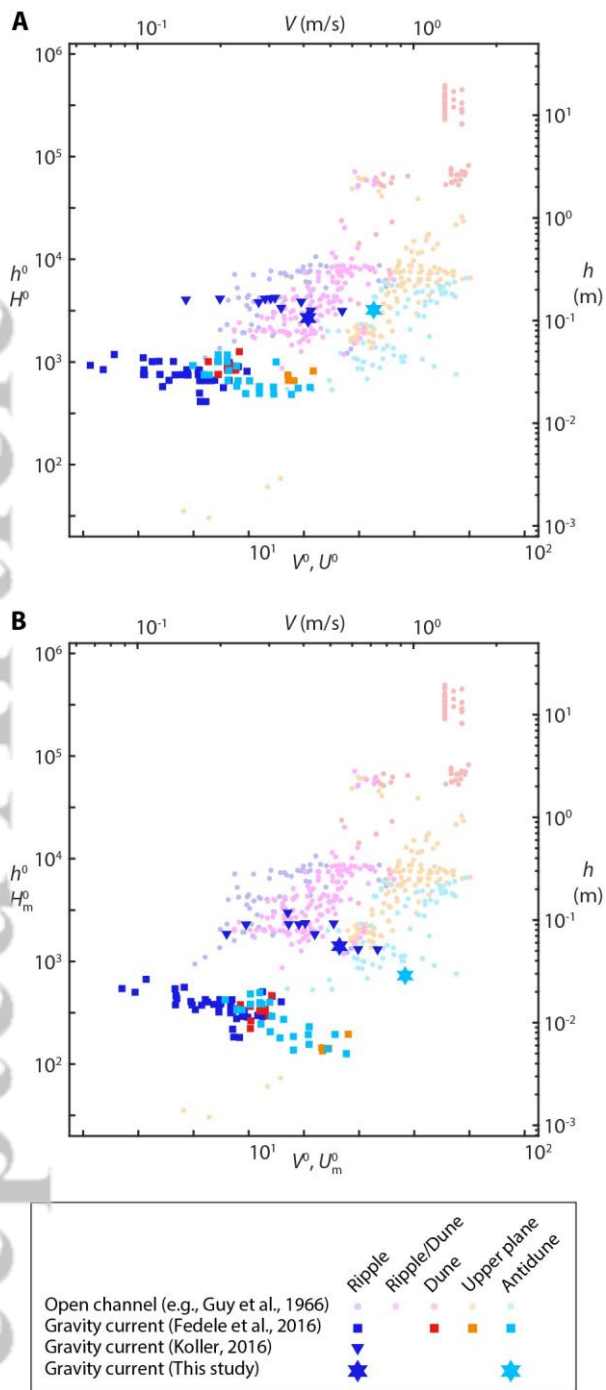


Figure 16 | Velocity-depth diagrams of bedforms for finer sediment ($Re_p, Re_{pg} \leq 11.37$). (A) Dimensionless flow thickness H^0 versus dimensionless flow velocity U^0 . (B) Dimensionless flow thickness of lower layer H_m^0 versus dimensionless maximum flow velocity U_m^0 .

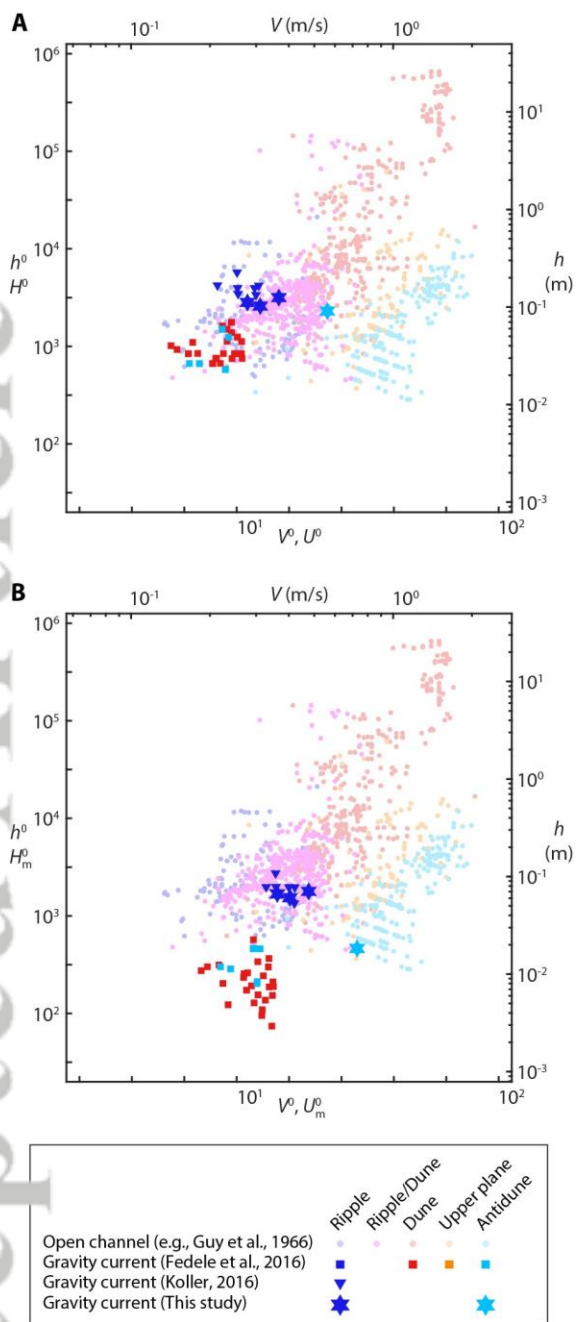


Figure 17 | Velocity-depth diagrams of bedforms for coarser sediment ($Re_p, Re_{pg} > 11.37$). (A) Dimensionless flow thickness H^0 versus dimensionless flow velocity U^0 . (B) Dimensionless flow thickness of lower layer H_m^0 versus dimensionless maximum flow velocity U_m^0 .

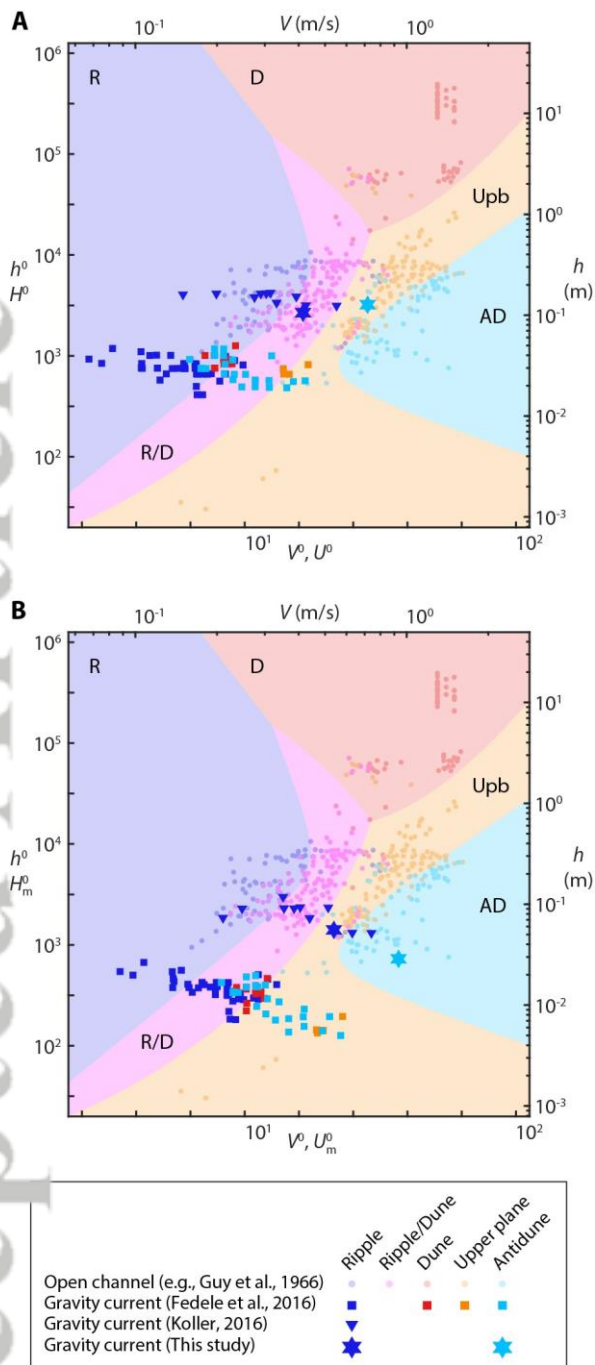


Figure 18 | Comparison of phase spaces of density-current bedforms with phase spaces of open-channel flow bedforms ($Re_p, Re_{pg} \leq 11.37$) obtained by the discriminant analysis. (A) Dimensionless flow thickness H^0 versus dimensionless flow velocity U^0 . (B) Dimensionless flow thickness of lower layer H_m^0 versus dimensionless maximum flow velocity U_m^0 .

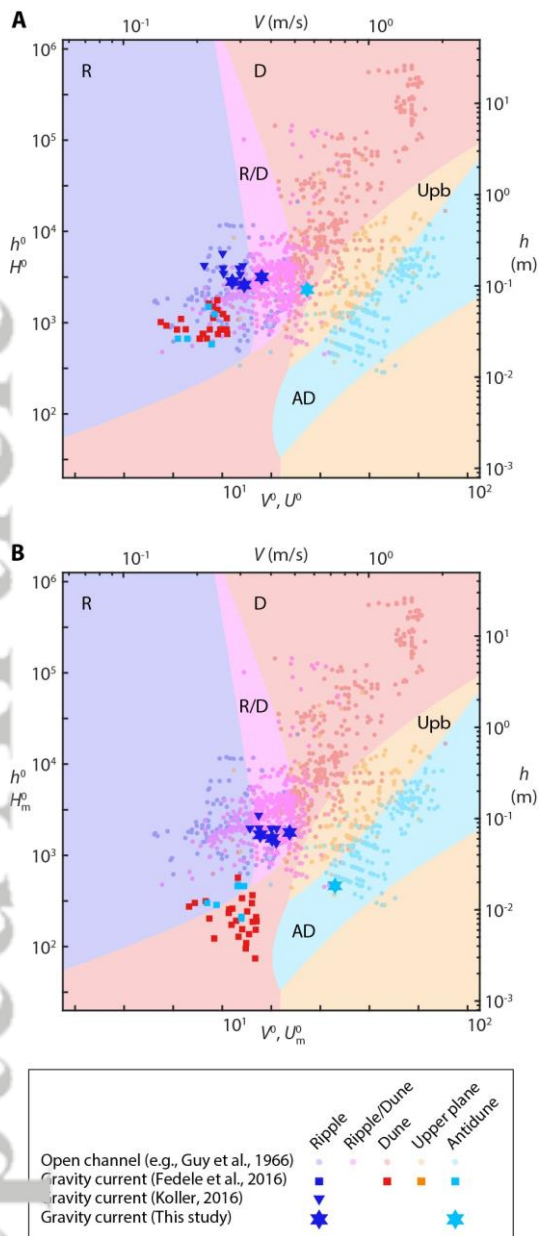


Figure 19 | Comparison of phase spaces of density-current bedforms with phase spaces of open-channel flow bedforms ($Re_p, Re_{pg} > 11.37$) obtained by the discriminant analysis. (A) Dimensionless flow thickness H^0 versus dimensionless flow velocity U^0 . (B) Dimensionless flow thickness of lower layer H_m^0 versus dimensionless maximum flow velocity U_m^0 .